Fermi National Accelerator Laboratory

FERMILAB-Conf-81/021-E

7420.180
(Submitted to Physica Scripta)

QUARK JETS FROM DEEPLY INELASTIC LEPTON SCATTERING*

Risto Orava

February 1981

*Presented at The Artic School of Physics, Lapland
July 27 - August 5, 1980

Operated by Universities Research Association Inc. under contract with the United States Department of Energy

Abstract

"Quark Jets From Deeply Inelastic Lepton Scattering" by R. Orava (Fermi National Accelerator Laboratory, P. O. Box 500, Batavia, Illinois, 60510, USA).

Physica Scripta (Sweden).

Experimental evidence for flavored spin-$\frac{1}{2}$ quarks in the nucleon as probed by the electromagnetic and weak currents is reviewed. Recent data on Q^2 dependence of the nucleon structure functions are presented and discussed.

Detailed structure of the hadron jets produced in deeply inelastic lepton-nucleon interactions is studied and evidence for the quark origin of the observed jets is presented.

1. Introduction

In the parton model of deeply inelastic lepton-nucleon scattering, a fast-moving nucleon is viewed as a bag of structureless partons which all travel in the same direction as the bound state hadron (Fig. 1a). These partons share the nucleon momentum and appear to the incoming point-like probe as free objects inside the rapidly moving nucleon (Impulse Approximation). The reaction rate is obtained as an incoherent sum over all contributing current-parton interactions.[1]

No free partons are observed, however, and it is conjectured that in a time-scale long compared to the time-scale of the current-parton interaction the parton struck by the current converts into the observed final state hadrons (Fig. 1b). The hadrons have their inclusive spectrum independent of the initial state (Environmental Independence) and the spectrum is determined only by the fragmenting parton and by the fraction of the parton energy carried by a hadron (Scaling).

The fundamental assumption of factorization of the inclusive hadron production rate into a current-parton interaction rate and a parton "hadronization" rate in the limit of large lepton momentum transfers, i.e., when $-q^2 \to \infty$, states[1]

$$\frac{d^2\sigma}{dxdz} \propto \Sigma_i \; F_i(x) D_i{}^h(z)$$

where x is the fraction of nucleon momentum carried by the parton i inside the nucleon and z fraction of the parton i momentum carried by the final state hadron h. The total inclusive production rate for hadron h from the parton i is then specified by the parton density distribution in the nucleon, $F_i(x)$, and the parton fragmentation function to hadrons, $D_i{}^h(z)$.

At the presently available, relatively low energies (as compared to the nucleon mass, for example) parton-parton final state interactions cannot be neglected; therefore, modifications to the simple, "instantaneous" picture of the nucleon are expected.

It is the purpose of these lectures (1) to review the evidence for spin-$\frac{1}{2}$ flavored quarks in the nucleon as probed by the weak and electromagnetic currents, (2) to present evidence for deviations from the simple quark-parton model as expected at finite (and low) energies, (3) to find evidence for the quark origin of jets observed in the final states of deeply inelastic lepton-nucleon interactions, and (4) to present a detailed study of the structure of the observed jets.

To introduce the restrictions imposed by the limited number of recorded interactions and by the systematics involved in the experimental measurements, I will start with a short description of the factors affecting any experimental analysis. Specifically, it will be seen that the two particle detection systems, the bubble chambers and the electronic detectors, are <u>complementary</u> devices in the measurement of the structure of the nucleon or in the study of the details of the hadronic final states.

1.1 <u>Experiments</u>

<u>Two Detectors</u>. Two basically different particle detection systems are employed in the studies of lepton-nucleon interactions at high energy. A large bubble chamber (10-20m^3) supplemented by an array of multi-wire proportional chambers for muon identification (EMI), (e.g., the 15-foot bubble chamber at Fermilab), provides a detailed description of each photographed event. Relatively small target mass (10-20 tons), however, leads to an inefficient usage of the available luminosity (L = no. of

beam particles per cm^2 and sec). Large electronic detectors (e.g., the apparatus of the Harvard-Pennsylvania-Wisconsin-Fermilab Collaboration (HPWF) at Fermilab) with a target tonnage of the order of 10^6 kilograms provide effective usage of the available luminosity. The electronic detectors are, however, blind to the details of the hadronic shower.

In Table I, I list characteristics of an "average" bubble chamber experiment and of an "average" counter experiment. The parameters quoted are imaginary and reflect, besides my prejudice, the complementary aspects of the two experimental setups. In a bubble chamber experiment, the final state muons, for example, are effectively identified down to 4 GeV/c laboratory momentum (P_L) at all angles relative to the direction of the incoming lepton (θ_L).

Momentum resolution ($\Delta P_L/P_L$) and the angular uncertainty ($\Delta\theta_L$) of the final state lepton in Table I are given for 100 GeV/c muons, and the hadronic energy resolution ($\Delta E_H/E_H$) for 100 GeV hadronic energy. Efficiency of a particular experimental setup is a combination of many different factors and is dominated by the scanning efficiency in a bubble chamber experiment. In an electronic counter experiment, the signal to background ratio and geometrical acceptance determine, together with the processing efficiency, the overall efficiency.

Complementarity of the two types of experiments is demonstrated by the different effective minimum values of the outgoing lepton momenta and the effective minimum hadronic energy deposit detected in the apparatus.

Statistics. A heavy target produces larger statistics and one may end up with as many as one hundred events for each bubble chamber event in an electronic counter experiment.

1.2 Free Quarks

Structure Functions. The dynamics of the current-nucleon interaction is contained in the three structure functions $F_i = F_i(Q^2,W^2)$ i=1,2,3 which correspond to different polarization states of the exchanged vector (axial vector) particle and to a parity violating interference term. The third structure function, $xF_3(Q^2,W^2)$ vanishes for the parity conserving electromagnetic processes.

Scaling. At sufficiently high energy where no intrinsic mass or length scale has relevance to the problem, $(W^2,Q^2\to\infty)$, the structure functions "scale", i.e., the value of a structure function F_i, measured at Q^2 and W^2 will be equal to the same F_i measured at other values of Q^2 and W^2, provided W^2 is scaled along with Q^2 (Bjorken scaling).

By definition, the scaling variable is then the Bjorken scaling variable $x = Q^2/2P\cdot q = Q^2/2M\nu$. Structure functions F_i may, in fact, behave in two ways for fixed W^2/Q^2:

(1) $F_i \to 0$

(2) $F_i \to F_i(x)$, finite

For elastic scattering, for example, $(x = Q^2/2M\nu = 1)$, $F_i\to 0$, when $Q^2\to\infty$. The parton model relates linear combinations of the structure functions to the parton densities in the nucleon, and thus for deeply inelastic scattering $F_i\to F_i(x)$, when $Q^2\to\infty$ (Impulse Approximation).

The Bjorken scaling hypothesis, based on current algebra, is then valid in the parton model as long as all the intrinsic mass scales, target mass, parton masses, primordial transverse motion, etc., are small compared to Q^2 or W^2.

Figure 2 shows the structure function F_2 as a function of Q^2 with $0.2<x<0.3$ as measured in an $\bar{\nu}$N-experiment[2], in a νN-experiment[3], and in

an electroproduction experiment[4]. No significant Q^2-dependence is observed.

Spin of the Charged Constituents. The Dirac cross section for elastic scattering of an electron by a spin-$\frac{1}{2}$ pointlike constituent with mass M, charge e, g=2 is

$$\frac{d\sigma}{dQ^2} = \frac{4\pi\alpha^2}{Q^4}\left\{ \left(1-y-\frac{My}{2E_o}\right) + \frac{y^2}{2} \right\} \qquad (1)$$

I compare this with the spin-averaged inelastic cross section in the scaling region for eN-scattering

$$\frac{d^2\sigma}{dQ^2dx} = \frac{4\pi\alpha^2}{Q^4}\left\{ \left(1-y-\frac{Mxy}{2E_o}\right) \frac{1}{x} F_2^{eN}(x_1Q^2) + \frac{y^2}{2}\, 2\, F_1^{eN}(x_1Q^2) \right\}$$

and get the Callan-Gross relation

$$\frac{F_2^{eN}(x) - 2\,x\,F_1^{eN}(x)}{2\,x\,F_1^{eN}(x)} = 0.$$

For spin-0 partons, the magnetic term in (1) is absent and $F_1^{eN}(x) = 0$, i.e.,

$$\frac{F_2^{eN}(x) - 2\,x\,F_1^{eN}(x)}{2\,x\,F_1(x)} \to \infty$$

For spin-1 partons, the cross section (1) is replaced by

$$\frac{d\sigma}{dQ^2} = \frac{4\pi\alpha^2}{Q^4}\,\frac{E'}{E_o}\left\{ \left(1+\frac{1}{3}\,\frac{Q^2}{2M^2}\right)\cos^2\frac{\theta}{2} + \left(1+\frac{1}{4}\sin^2\frac{\theta}{2}\right)\left(\frac{Q^2}{3M^2}\sin^2\frac{\theta}{2}\right) \right\}$$

which does not scale.

Electro- and muoproduction experiments have been used to determine $R \simeq (F_2(x) - 2xF_1(x))/2xF_1(x)$ and yield $R^{eN} = 0.20 \pm 0.07$ (Ref. 6), $R^{\mu N} = 0.44 \pm 0.25 \pm 0.04$ (Ref. 7).

The HPWFRO Collaboration measured $R^{\nu N} = 0.11 \pm 0.07$ (Ref. 5).

Flavor of the Partons. To proceed, I need a model for weak

interactions. In the Weinberg-Salam model that incorporates the so-called GIM-mechanism, the charged currents are left-handed and left-handed quarks and leptons are grouped into doublets. Right-handed quarks are in singlets. The dominating process in neutrino (antineutrino) charged current interactions is then $\nu d \to \mu^- u$ ($\bar{\nu} u \to \mu^+ d$).

Couplings of the weak currents are thus more "selective" than the coupling of the electro-magnetic current. For electroproduction

$$\begin{aligned} F_2^{eN}(x) &= \Sigma_i e_i^2 (q(x) + \bar{q}(x)) \\ &= \frac{1}{2} (F_2^{ep}(x) + F_2^{en}(x)) \\ &= \frac{5}{18} x \{ V(x) + O(x) + C(x) \} + \frac{1}{6} x \Delta^{eN}(x), \end{aligned}$$

where $\Delta^{eN}(x) = (\bar{c}(x) - \bar{s}(x)) + (c(x) - s(x)) = C(x) - S(x)$.
The weak structure functions $F_i(x)$ are related to the spin-$\frac{1}{2}$ quark densities as follows:

$$F_2^{\nu,\bar{\nu}}(x) = x (V(x) + O(x) + C(x))$$

$$x F_3^{\nu,\bar{\nu}}(x) = x V(x) \pm x\Delta^{eN}(x) ,$$

where $V(x)$, $O(x)$ and $C(x)$ are the valence, noncharmed ocean and the charmed ocean distributions, respectively.

The quark-parton model then predicts the following flavor-relation between F_2^{eN} and $F_2^{\nu,\bar{\nu}}$:

$$F_2^{eN} = \frac{5}{18} F_2^{\nu,\bar{\nu}} + \frac{1}{6} x \Delta^{eN}(x) .$$

This prediction depends crucially on the fractional charges of quarks. Assuming, for example, that u and d form an isodoublet with charged +1 and 0 we would find

$$F_2^{eN} \simeq \frac{1}{2} F_2^{\nu,\bar{\nu}} .$$

Figure 3 shows experimental data on F_2 in an $\bar{\nu}N$-experiment[2], in a νN-experiment[3], and in an ed-experiment[4] multiplied by a factor of $\frac{18}{5}$. The prediction obtained from the ed-results by assuming an isodoublet for u- and d-quarks is shown by a dashed line. The data clearly favors the fractionally charged quarks.

Other Partons Than Quarks? Assuming that $x\Delta^{eN}=6(F_2^{eN}(x)-\frac{5}{18}F_2^{\nu,\bar{\nu}}(x))$ is small, we obtain the valence quark distribution $xV(x)$ as $xV(x) \simeq xF_3^{\nu,\bar{\nu}}(x)$.

The number of valence quarks in the nucleon, n_v, is then obtained as the integral

$$\int_0^1 x \frac{F_3(x)}{x} \, dx \simeq n_v$$

(Gross-Llewellyn Smith Sum Rule). The values of n_v as obtained by the CDHS Collaboration[8] with different lower limits for the integration, x_{min}, are shown in Fig. 4. The dashed line represents a parametrization of $xF_3(x)$ for all x.

Experimental Reality. The number of valence quarks obtained as the integral n_v depends, however, crucially on the x_{min} value accessible to the experiment. The HPWFRO Collaboration finds that half of the integral n_v, in their experiment, comes from the first bin.

In fact,

$$\Delta x = \Delta\theta \sqrt{\frac{2E}{M}\frac{1-y}{y}} \sqrt{x} \quad .$$

Below some critical value, x_c, the error in x becomes larger than the x-value ($\Delta x \simeq x$ at $x=x_c$), and clearly $x_c \propto (\Delta\theta)^2$. On the other hand, $\Delta\theta \sim 0.25/\text{length of } \mu$, i.e., $x_c \propto 0.06/(\text{length})^2$.

In Table II, I list the experimental results for n_v as obtained in various neutrino-experiments. The results are consistent with $n_v=3$, but depend on x_{min}.

The momentum carried by the valence quarks is given by $I_3=\int xF_3dx$ and the momentum carried by all the quarks in the nucleon by $I_2=\int F_2dx$. If there would be only charged quarks in the nucleon, then $I_2=1$. In Table III, I list the experimental results for I_2 and I_3 in different neutrino experiments. The corresponding result for I_2 obtained in an eN experiment is $I_2^{eN} = 0.15 \pm 0.01$. From Table III, we see that less than 50% of the nucleon momentum is carried by the charged quarks. There, again, one should keep in mind the different x_{min} values accessible to an experiment.

Valence Quark Distribution. If I do not neglect the $\Delta^{eN}(x)$ term in the expression for the valence quark distribution xV(x), I find

$$xV(x) = \frac{1}{2}\,(xF_3^{\nu}(x) + xF_3^{\bar{\nu}}(x)) \quad .$$

A parametrization often used for xV(x) is of the form $xV(x) = Vx^A(1-x)^B$, where the parameters A and B are suggested to be $A \sim 1/2$ and $B \sim 3$ by Regge Theory and by the quark counting rules. The HPWFRO Group finds for A and B, $A=0.87 \pm 0.07$ and $B=3.40 \pm 0.02$, with neutrino energies of $20<E_0<220$ GeV (Fig. 5).[5]

Ocean Quark Distribution. I define

$$B^{\nu,\bar{\nu}} = I_3/I_2 = \int x\,F_3^{\nu,\bar{\nu}}dx/\int F_2^{\nu,\bar{\nu}}dx$$

$$= V \pm \Delta^{eN} \;/\; (V+O+C) \quad ,$$

where $V=\int xV(x)dx$, $O=\int xO(x)dx$ and $\Delta^{eN}=\int dx\; x\; \{(\bar{c}(x)-\bar{s}(x))+(c(x)-s(x)\}=C-S$. Using the results $I_2^{eN}=0.15\pm0.01$, $I_2^{\nu N}=0.44\pm0.02$, I get $\Delta^{eN}=6(I_2^{eN}-\frac{5}{18}\,I_2^{\nu N}) = 0.18\pm0.02$. From the direct measurement of Δ^{eN}, on the other hand, $\Delta^{eN}=C-S=\frac{1}{2}(B^{\nu}-B^{\bar{\nu}}) = \frac{1}{2} \times (0.07\pm0.02) = 0.04\pm0.01$ (Ref. 5).

Assuming the symmetry $O=\bar{O}$, $C=\bar{C}$, I find

$$1-B^{\bar{\nu}} = \frac{O+S}{V+O-C} = 2\,\frac{\bar{O}+\bar{S}}{V+O+S}$$

and

$$1 + B^{\bar{\nu}} = \frac{2V+\bar{O}+2C-S}{V+\bar{O}+C} = \frac{V+\bar{O}+2\bar{C}-\bar{S}}{V+\bar{O}+C}$$

and thus

$$\frac{1}{2}(1-B^{\bar{\nu}}) = \frac{\bar{O}+\bar{S}}{V+\bar{O}+C}$$

then

$$\frac{1-B^{\bar{\nu}}}{1+B^{\bar{\nu}}} = \frac{\bar{O}+\bar{S}}{V+\bar{O}+2\bar{C}-S} = \frac{\bar{O}+\bar{S}}{Q+2C} \quad ,$$

where

$$Q = \int x \{(u_V(x) + d_V(x) + u_O(x) + d_O(x)\}\, dx$$

Strange Ocean. Production of opposite sign di-muon events occurs in antineutrino charged current events from the transitions $\bar{s}\rightarrow\bar{c}$, and the cross section should then be proportional to the strange quark distribution $\bar{s}(x)$.

Using antineutrino charged current di-muon data and antineutrino charged current y-distribution data, one obtains

$$\frac{2\int x\bar{s}(x)dx}{\int x\,(V(x)+C))dx} = \frac{\sigma(\mu^+\mu^-)}{\sigma(\mu^+)} \quad \frac{\varepsilon}{Br} \quad (\frac{1}{3} + \frac{1-B^{\bar{\nu}}}{1+B^{\bar{\nu}}})$$

which probes the strange ocean x-distribution (Table IV). Br is the branching ratio $\bar{c}\rightarrow\mu^-$ and is taken to be Br=0.08±0.03; ε is the acceptance correction needed for the di-muon events.

Conclusions.

1) There are partons in the nucleon which couple to the weak and electromagnetic probes.

2) The partons probed by weak and electromagnetic currents are spin-$\frac{1}{2}$ particles.

3) The partons probed by weak and electromagnetic currents are quarks.

4) There are approximately three valence quarks in the nucleon.

5) About half of the nucleon momentum is carried by neutral partons which do not couple to the weak or electromagnetic probes.

6) The quark-antiquark ocean in the nucleon is not SU(3) symmetric: $\bar{s}/\bar{u} \neq 1$ (see Table IV).

2. An Experimental Observation

The data on structure functions $F_i(x)$ show Q^2-dependence at small x-values ($x \lesssim 0.05$) and at large x-values ($x \gtrsim 0.50$). The Q^2 dependence of the structure functions in neutrino-[3,8], antineutrino-[2], muon-, and in electron-nucleon experiments is confined to relatively low Q^2-values (low compared to the internal mass scales in the problem) (Fig. 6).

At moderate x-values, there is no significant Q^2-dependence in the structure functions. This observation was dubbed precocious scaling, i.e., scaling at low W^2 and Q^2 as compared to the intrinsic mass scales. There is a rise in F_2 with increasing Q^2 at small x and there is a drop in F_2 with increasing Q^2 at large x. There is also an indication of a drop in xF_3 with increasing Q^2 at large x. Does the data thus show precocious scaling violations?

2.1 Experimental Realism

The x-range explored is different in different experiments. This is understood in terms of acceptance and statistics of a particular experimental setup. The minimum accessible x-value is theoretically defined as $x_{min}=Q^2/2M\nu_{max}$ for a given Q^2. The minimum effective x-value is given, however, in terms of the uncertainty in the muon angle relative to the beam direction, $x_{min}^{eff} \propto (\Delta\theta)^2$ (see Lecture I). Moreover, the energy measurements may shift the whole x-distribution since $x=E_0E'\theta^2/2M\nu$. Large x-values are especially vulnerable to the systematic errors. In Figure 7 are given the theoretical kinematical regions of the

Fermilab 15-foot bubble chamber experiments, the CDHS electronic counter experiment and the SLAC eN-experiment, with the effect of the selection $W \geq 2$ GeV to the kinematical range also shown.

Experimental resolution is finite. Therefore, the measured distributions are smeared. De-smearing functions for the quantity x, $\varepsilon(x) = G^{true}(x)/G^{smeared}(x)$, where $G^{true}(x)$ and $G^{smeared}(x)$ are calculated from a Monte Carlo program with varying input assumptions (Fig. 8). The Monte Carlo program also "includes" the experimental conditions. These input assumptions necessarily dilute the credibility of an experiment in the regions where there is a need for a significant correction to the data. One thus needs cross checks of the measured quantities. Here, again, the tails of the measured distributions are most vulnerable to the systematics. Smearing effectively defines the maximum x-values accessible to an experiment.

Finally, uncertainties in the incident lepton flux, corrections due to lepton and target bremsstrahlung radiation, and uncertainties due to the nucleon Fermi motion affect the detailed shape of the measured structure functions $F_i(x,Q^2)$.

2.2 Large-x Phenomena

I assume, for the moment, that we as experimentalists understand the experimental features of the data. (Many theorists, in fact, do make this assumption!) Then the experimentally observed decrease of the structure functions at large-x as a function of Q^2 should be interpreted as a decreasing contribution of the valence quarks in the nucleon.

Figure 9 shows the ocean quark distribution $xO(x) \sim F_2^{\nu N} - xF_3^{\nu N}$ measured by the CDHS-Group[8] as a function of x and Q^2. The wide-band data shows an increasing trend at small x-values as a function of Q^2 in

accordance with the expectation.

Elastic Scattering. For elastic scattering $W^2 \equiv M^2$ and since $W^2 = Q^2(1/x-1)+M^2$ then $x=1$. Figure 10 shows $F_2^{en}-F_2^{ep}$ for inelastic eN scattering together with the elastic peak at $x=1$ (Ref. 4).

Quasi-elastic Scattering. The reaction $\nu p \to \mu^- \Delta^{++}$ represents about 7% of all νp charged current interactions - other exclusive channels represent about 20% of the cross section.

No scaling in x (in Q^2/W^2) is expected near a resonance. The cross section at a resonance is proportional to a Breit-Wigner function (BW) multiplied by a form factor (f),

$$\sigma_{ReS} \sim BW\,(W^2) f(Q^2) \quad .$$

The Breit-Wigner function is given, for example, as

$$BR(W^2) = \frac{W_R\,\Gamma/\pi}{(W^2-W_R{}^2)^2+W_R{}^2\Gamma^2} \quad ,$$

where Γ is width of the resonance and W_R is the mass of the resonance.

The vector part of the cross section for the reaction $\nu p \to \mu^- \Delta^{++}$ vanishes in the forward direction $Q^2 = 0$, $\sigma_V(\nu p \to \mu^- \Delta^{++})|_{Q^2=0} = 0$, by current conservation.

Q^2-dependence. The differential cross-section is given as

$$\frac{d^2\sigma}{dQ^2dW^2} = \frac{G}{16\pi M^2}\,(k_1W_1+k_2W_2+k_3W_3) \quad .$$

where k_1, k_2, and k_3 are kinematical factors which contain the dependence on the incident energy. W_1, W_2, and W_3 are structure functions $W_i = W_i(W^2,Q^2)$,

$$W_i \propto BR(W^2)\ \Sigma_i\ C_i^{V,A}(Q^2) \quad .$$

The functions $C_i^{V,A}(Q^2)$ are vector and axial vector form factors given by Rarita and Schwinger. Explicit parametrizations for $C_i^{V,A}(Q^2)$ are often used,

$C_3^V(Q^2)^2 \propto Q\exp(-6.3Q)$, $C_4^V = -\frac{M}{W} C_3^V$, $C_5^V = 0$, $C_i^A(Q^2) = C_i^A(0)\{1+aQ^2/(b+Q^2)\}/\{1+Q^2/M_A^2\}^2$ for i = 3,4,5 and $C_6^A(Q^2) = -(g_\Delta f_\pi M)/\{2\sqrt{3}(m_\pi+Q^2)\} \times 1/\{1+Q^2/M_A^2\}^2$, where g_Δ is the $\Delta^{++}\to p\pi^+$ coupling constant and f_π the pion decay constant.

One may use the eN data and CVC to fix the matrix element $\langle\Delta^{++}|V|p\rangle$. The axial vector part $\langle\Delta^{++}|A|p\rangle$ contains the unknown parameter M_A with the dimensions of mass. Figure 11 shows the energy dependence of the cross section $\sigma(\nu p\to\mu^-\Delta^{++})$.[3] A fit to the total cross section over the energy range E_o=20-200 GeV gives for M_A=0.85±0.10. Figure 12 shows the Q^2-dependence of the process with model estimates for the vector, axial vector and interference parts of the cross section.

Target Mass Effects. Neglecting the mass of the initial quark, we obtain in the limit $Q^2 >> m_f^2$

$$x \to \xi = \frac{Q^2}{M(\nu+\sqrt{\nu^2+Q^2})}$$

which is the so-called Nachtmann scaling variable. A change in the scaling variable only affects the small Q^2 large-x region.

Other Mass Scales. By the Uncertainty Principle, the constituents confined into the nucleon dimensions have "primordial" motion. Structure functions will then "scale" according to a new variable, ξ, which accounts for this primordial transverse motion, k_T. To the first order in $\langle k_T^2\rangle/Q^2$,

$$\xi = \xi\,(1+C\langle k_T^2\rangle/Q^2)$$

and

$$F(\xi) = F(\xi) + C\frac{\langle k_T^2\rangle}{Q^2} F'(\xi) + \ldots$$

"diffractive" $c\bar{c}$-pair production in muon-nucleon interactions[9]. Diffractive production $\mu N \to \mu(c\bar{c}) + X$ is here defined as fast $\mu^+\mu^-$ pairs produced forward in the current direction. The data sample consists of 20,000 di-muon events obtained with 209 GeV incident muons in the Fermilab Multi-Muon Spectrometer. About 80% of the di-muon events are estimated to be coming from $c\bar{c}$ production. The cross section for the process is in agreement with the Photon-Gluon Fusion Model. The total cross section for diffractive chain production is measured to be $6.9^{+1.9}_{-1.4}$ nb. The structure function $F_2(c\bar{c})$ is defined by

$$Q^4 \nu \frac{d^2\sigma(c\bar{c})}{dQ^2 d\nu} = 4\pi\alpha^2 \left(1-y+\frac{y^2}{2}\right) F_2(c\bar{c}) \quad .$$

Here $F_2(c\bar{c})$ plays the same role in charm production as would $F_2(x,Q^2)$ in inclusive scattering if absorption of longitudinally polarized photons were negligible.

Note that in vector meson dominance model, the Q^2-dependence of F_2 at x=o would be roughly

$$\frac{F_2(c\bar{c})}{F_2(Q^2,x)}\Big|_{x=o} = \frac{2}{3}\,\frac{Q^2+M_\rho^2}{Q^2+M_\psi^2} \quad ,$$

where the factor 2/3 comes from the squared quark charges.

Table 5 shows how much of the overall Q^2-dependence in the total $I_2^{\mu N}$ is coming from the $c\bar{c}$ production. On the average, for Q^2 values of $1<Q^2<13$ GeV^2, about 30% of the Q^2-dependence is seen to be due to the "diffractive" $c\bar{c}$-production.

Heavy Quark Thresholds. If the final state quark mass is accounted for, the scaling variable will be approximately (light-to-heavy quark transition) $x \to x+m_f^2/2M\nu$, where m_f is the final state quark mass. Then the structure function $F_2(x)$ is transformed to $F_2(x) \simeq F_2(x+m_f^2/2M\nu)$. With

new heavy quark production, the small x-values (and large y-values) will be populated first.

Conclusions. Confinement of the nucleon constituents affects the structure functions at Q^2-values of a few GeV^2. Confinement effects behave as powers of Q^2. The following problems are important:

At large x-values: (1) Experimental uncertainties, (2) Elastic scattering, (3) Quasi-elastic scattering, (4) Target mass effects, (5) Primordial k_T of partons, (6) Di-quark scattering.

At small x-values: (1) Experimental uncertainties, (2) Diffractive processes, (3) Heavy quark thresholds.

One should note that this discussion has been based on phenomenological models and kinematics and not on theory.

2.4 Asymptotically Free Quarks

Quarks are colored. This is a colloquial way of saying they have a new quantum number label and is known from spectroscopy (e.g., Ω^- or Δ^{++}), e^+e^-- annihilation to hadrons (R) and elsewhere (π^o lifetime, Drell-Yan processes). Gluons, found in excess compared with charged partons in the nucleon, couple to the color-charge of quarks. The colored coupling strength is independent of quark flavor, but depends on the resolution of the probe determined by Q^2. At large Q^2, the leading logarithm summation gives the coupling ($Q^2 >> M_Q^2$), $\alpha_s^o = g^2/4\pi = \frac{12\pi}{(33-2n_f)\ln(Q^2/\Lambda^2)}$. Therefore, quarks are asymptotically free if $n_f<17$.

A non-singlet structure function is a structure function to which only quark operators contribute. A singlet structure function is a structure function to which both quark and gluon operators contribute. For example, gluons are neutral and thus $F_2^{ep} - F_2^{en}$ is a non-singlet, or because gluons have definite G-parity and V and A currents have opposite charge conjugation xF_3 is a non-singlet.

Q^2-Evolution. In the simple parton model $Q^2 \frac{\partial F_2}{\partial Q^2} = 0$.

In QCD the Q^2-variation of a non-singlet structure function arises, in the leading order, from a single gluon Bremsstrahlung diagram and can be expressed by the recursive equation of Altarelli and Parisi[10],

$$Q^2 \frac{\partial}{\partial Q^2} xF_3(x,Q^2) = \frac{\alpha_s^o(Q^2)}{2\pi} \int_x^1 dw \frac{x}{w^2} wF_3(w,Q^2) P_{qq}(\frac{x}{w}) \quad .$$

Here, P_{qq} is a splitting function which represents the probability of finding a quark of momentum fraction x arising from a quark of momentum fraction w, when probed with momentum Q^2.

The splitting functions can be calculated in QCD. Substituting P_{qq} in the Altarelli-Parisi equation, we get:

$$Q^2 \frac{\partial}{\partial Q^2} xF_3(x,Q^2) = \frac{\alpha_s^o(Q^2)}{3\pi} \{(3-4\ln(1-x))\ xF_3(x,Q^2) + \int_x^1 dw \frac{2}{(1-w)} ((1+w^2)\frac{x}{w} F_3(\frac{x}{w},Q^2) - 2xF_3(x,Q^2))\} \quad .$$

Given xF_3 at $Q^2=Q_o^2$ equation determines the Q^2-evolution.

Boundary Condition? The problem of setting a proper boundary condition for the equation is related to the experimentally available x-Q^2 range. No experiment measures the full xF_3 at a given Q^2-value.

A way to solve the problem is to parametrize the data, for example, $xF_3(x,Q_o^2) = C\ x^A(1-x)^B$ at a reference value $Q^2=Q_o^2$, thus defining the boundary condition. We have seen that the experimental data gives roughly A=1/2, B=3. The parametrization will restrict the predictive power of QCD.

Magic of the Moments. To get the moments of xF_3, I multiply the leading order equation by x^{n-2} and integrate over x. A more formal

approach sums all the leading logarithms of QCD perturbation theory, i.e., terms of the order $(\alpha_s \ln Q^2)^n$. Corrections of the order $\alpha_s^n (\ln Q^2)^{n-1}$ are neglected. The moments of the non-singlet structure functions are

$$M^{ns}(n,Q^2) = M^{ns}(n,Q_o^2) \left\{\frac{\alpha_s^o(Q^2)}{\alpha_s^o(Q_o^2)}\right\}^{d_n} ,$$

where

$$d_n = \frac{4}{33-2n_f}\left(-1 + \frac{2}{n(n+1)} - 4\sum_{j=2}^{n}\frac{1}{j}\right)$$

are the anomalous dimensions, i.e., w^n-moments of the Gluesstrahlung vertices P_{qq}.

Using Eq. 1 for $\alpha_s^o(Q^2)$, we get $M^{ns}(n,Q^2) = \frac{C_n}{(\ln Q^2/\Lambda^2)^{d_n}}$ with C_n unknown constants to be determined from the data. The uncertainty in the boundary conditions does not appear when dealing with moments. However, experiment measures only a fraction of the structure functions at a given Q^2-value. (As we have seen earlier in Part I, half of the integral over $F_3(x)$ comes from the very first bin in the HPWFRO experiment. One has to extrapolate the data to x=0, i.e., when evaluating the moments $M(n,Q^2) = \int dx\, x^{n-2} xF_3(x,Q^2)$ one assumes the shape of xF_3: $\sim (1-x)^3$.

Experimentally known fractions of the moments $M(n,Q^2)=\int dx\, x^{n-2} xF_3(x,Q^2)$ in the CDHS experiment[8] are

Q^2 GeV^2	n = 2	3	4	5	6
4	53%	30%	15%	12%	3%
6	72%	53%	34%	21%	12%
10	92%	87%	77%	65%	54%
20	80%	92%	91%	86%	79%
45	54%	77%	86%	86%	81%
75	32%	56%	71%	77%	77%

Determination of Λ. In the leading order perturbative QCD, one may write: $M^{ns}(n,Q^2)^{-1/d_n} = C_n^{-1/d_n} \ln Q^2/\Lambda^2 = C_n'' (\ln Q^2 - \ln\Lambda^2)$ and one can determine Λ by plotting $M^{-1/d}$ as a function of Q^2. Next to the leading order corrections were absorbed into Λ and therefore Λ becomes function of n, i.e., $\Lambda \to \Lambda_n$ (Fig. 14).

Higher Order Corrections. Including next to the leading order corrections $O(\alpha_s)$, the QCD prediction is modified to be

$$M^{ns}(n,Q^2) = \frac{C_n}{(\ln Q^2/\Lambda^2)^{d_n}} \left(1 + \frac{A_n + B_n \ln\ln Q^2/\Lambda^2}{\ln Q^2/\Lambda^2}\right) ,$$

where the coefficients A_n and B_n are calculated in perturbation theory. The colored coupling is not uniquely defined, but depends on the particular "renormalization scheme"; different QCD predictions for the same quantities may result.

One may absorb next to the leading order corrections into the physical parameter Λ , $\Lambda \to \Lambda_n$, i.e.,

$$M^{ns}(n,Q^2) = \frac{C_n'}{(\ln Q^2/\Lambda_n^2)^{d_n}} .$$

Log-Log Plots. Taking logarithms on both sides of the moment equation one gets: $\ln M^{ns}(n,Q^2) = \ln C_n - d_n \ln(\ln Q^2/\Lambda^2)$. By plotting different moments against each other, one should find the data lie on straight lines with slopes equal to the ratio between the corresponding anomalous dimension d_n/d_m (Fig. 15).

Further Twists. At low energies ($Q^2 \sim M^2$)the fact that quarks are not free but bound to the hadronic wave functions shows up as we have seen earlier. The mass scale can be defined by any of the discussed possibilities: resonance production, primordial quark motion, di-quark scattering, etc.

These effects were seen to behave as $(M^2/Q^2)^n$, i.e., to decrease

as powers of Q^2.

The perturbative QCD predictions are then modified by typically non-perturbative effects ($\alpha_s(Q^2) \gtrsim 1$),

$$M^{ns}(n,Q^2) = \frac{C_n}{(\ln Q^2/\Lambda^2/^d n} \left(1 + \frac{A_n + B_n \ln\ln Q^2/\Lambda^2}{\ln Q^2/\Lambda^2}\right) *$$

$$*\left(n\, t_n \frac{M^2}{Q^2} + ..\right)$$

3. Parton Fragmentation

Two characteristic features of hadron fragmentation in particle production observed in hadron-hadron interactions at high energy are the existence of a flat plateau in rapidity and the retention of hadron quantum numbers, on the average, in the hadron fragmentation region. Berman, Bjorken, and Kogut have argued that parton fragmentation should also develop a plateau[11] and Feynman has suggested that the quantum numbers of the quark-parton are also retained, on the average, in the quark fragmentation region.[1]

Gross features of the jets produced by parton fragmentation are, at present energies, well described by the parametrization of Field and Feynman who assume (i) simple momentum sharing in the quark fragmentation process, (ii) the size of SU(3) symmetry violation, and (iii) the spin nature and the limited transverse momentum of the primary mesons.[12]

I want to emphasize that most of the experimental tests have been, however, insensitive to the basic hypothesis that quark fragmentation is the origin of the observed hadron states.

It is the purpose of this lecture to present evidence for the quark origin of the hadron jets in deeply inelastic leptoproduction and to provide a detailed description of the structure of the observed jets.

This is important not only to learn how quarks turn into the observed hadron states, but it is also a necessary condition--as we shall see--for forthcoming QCD-tests.

3.1 Jet Definition

Detailed consideration of the rapidity distribution of the hadrons resulting from the deeply inelastic interactions is given by Bjorken; he separates the following distinct rapidity regions (Fig. 16):[12]

(1) Particles moving rapidly forward in the current direction in the hadron c.m.s. arise from the fragmentation of the quark which the current has knocked out of the target nucleon (Region V).

(2) Particles moving to the opposite, backward, direction relative to the current direction in the hadron c.m.s. lie in the target fragmentation region and arise from the "hadronization" of the partons which remained after the collision (Region I).

(3) Particles moving slowly with respect to the c.m.s. lie in the central region (target plateau, Region II, and current plateau, Region IV). Their distribution is flat in rapidity. The central region also contains the region of phase space formerly occupied by the struck quark before it was removed (the hole fragmentation region, Region III).

The rapidity in the c.m.s. is $y^*=1/2\ \ln\{(E^*+P_L^*)/(E^*-P_L^*)\}$, where E^* is the hadron c.m.s. energy and P_L^* the hadron c.m.s. momentum along the current direction. The length of the total rapidity interval is proportional to $\ln W^2$, while the length of the current fragmentation region is proportional to $\ln Q^2$. Hence, one should select relatively large values of W and Q^2 to ensure adequate separation of the target and current fragments.

The net charge distribution of the hadrons, $(1/N_{ev})d(N^{+}-N^{-})/dy^{*}$, where N_{ev} and $N^{\pm}$ are the numbers of events and charged tracks, respectively, can be used to show that in the hadron c.m.s. the current jet is most readily separated. As variables for the inclusive distributions, we use either the c.m.s. rapidity y^{*}, or the fractional energy in the laboratory system ($z=E_h/\nu$, where E_h is the hadron energy). To define the current jet, we transform the hadron four vectors into the hadronic c.m.s. and require that the c.m.s. rapidity of each hadron is positive, i.e., $y^{*}>o$. In the following, we shall select $x>0.1$ to investigate the predictions for d-quark (u-quark) jets in $\bar{\nu}(\nu)$-N interactions.

3.2 Fragmentation Functions

Factorization. In the quark-parton model of deeply inelastic scattering, the inclusive one-particle cross section is written as a product of the nucleon structure functions, $F_i(x)$, and the quark-parton (p_i) fragmentation functions, $D^{h}_{p_i}(z)$, to a hadron h of fractional momentum z, i.e., in the limit $Q^{2}\to\infty$

$$\frac{d^{2}\sigma}{dxdz} = \frac{G^{2}ME}{\pi} \sum_{i=i}^{n_f} F_i(x)\, D^{h}_{pi}(z) \quad ,$$

where n_f is the number of quark flavors (factorization hypothesis)[1].

We define the fragmentation function $D^{h}_{p_i}(z)$ with a given Q_o^{2}-interval in different intervals of x,x_i, as follows:

$$D^{h}_{p}(z,Q^{2}_{o},x_i) = \frac{1}{N_{ev}} \frac{dN^{tracks}}{dz} \Big|_{x_i,Q^{2}_{o}}$$

where N_{ev} and N^{tracks} denote the number of events and tracks, respectively. The ratio $R = D^{h}_{p}(z,Q^{2}_{o},x_i)/D^{h}_{p}(z,Q^{2}_{o},x_j)$ where $i \neq j$, should then show deviation from a constant value if the factorization hypothesis is violated.

Figure 17a shows the ratio R plotted with $3<Q_o^2<10$ GeV$^2/c^2$ for two average values of x, $\langle x_1\rangle=0.1$ $(0.01<x_1<0.20)$ and $\langle x_2\rangle=0.2$ $(0.1<x_2<0.3)$. No factorization violation is observed in the region where one can safely speak about the current fragments ($z>0.2$). The factorization property of the inclusive one-particle cross section is further demonstrated in Figures 17b,c where different average x-values were chosen. Our results for the one-particle distributions show no significant x-dependence.

Isospin Conservation. Isospin conservation in any quark jet implies the relation for the quark fragmentation functions, $D_p^{\pi^+}(z) + D_p^{\pi^-}(z) = 2D_p^{\pi^o}(z)$ independent of the initial process, x or y. Figure 18 shows experimental data for the fragmentation functions $D_p^h(z)$ in four different experiments. Since pion production consists of about 90% of all final state particles, the isospin relation is expected to hold approximately. The data is seen to be consistent with this expectation.

Isospin Symmetry. Isospin symmetry among the quarks u and d implies $D_u^{\pi^\pm}(z) = D_d^{\pi^\mp}$, which is tested in Figure 19 by neutrino and antineutrino data. The data for the processes $\bar{\nu}N\to\mu^+h^+X$ is corrected for the proton contamination by using the spectrum of observed lambda-hyperons. The data are compared with the parametrizations of Field and Feynman[12] which are seen to agree well with the experimental results.

Particle Ratios. The ratio $h^-/h^+ = D_d^{h^-}(z)/D_d^{h^+}(z)$ should approach infinity as z approaches one for the genuine d-quark jets. We test this hypothesis in Figure 20 and find a good agreement with the Field and Feynman parametrizations for the fragmentation functions which are obtained using the SU(3)-symmetry violation parameter of 0.27 instead of 0.5 originally chosen by Field and Feynman. The ratio h^-/h^+ stays

constant as a function of Q^2 and P_T^2 ruling out a significant resonance contribution. No threshold behavior or dependence on Q^2 is seen.[13]

The ratio K^o/h^- measures the relative suppression of the strange quark-and-quark pairs generated in the quark jet. Resonance contributions are expected to die out as z approaches one. Assuming that it is the d-quark which dominantly fragments to hadrons in $\bar{\nu}N$ charged current interactions, there cannot be any primary $\bar{K}^o$'s or K^-'s in the jet. Figure 21 shows the ratio

$$K^o/h^- = \int_{z_{min}}^{1} D^{K^o}(z)dz / \int_{z_{min}}^{1} D^{h^-}(z)dz$$

plotted as a function of z_{min}. Leaving the size of the SU(3) symmetry violation as a free parameter in the Field and Feynman parametrization of the d-quark fragmentation functions, we get the predictions shown by the solid lines in Figure 21. The measurement gives for the SU(3)-symmetry violation in the d-quark jets, Ps/p = 0.27±0.04 (Ref. 14).

3.3 Jet Quantum Numbers

Quark quantum numbers are not necessarily retained in the current fragmentation region, but space-time structure of the fragmentation process limits possible models to ones which contain the quark quantum retention--modulo a small leakage factor. The leakage of quark quantum numbers is illustrated in Figure 22 for meson and baryon production.

Denoting the probabilities of finding a quark of flavor i in the quark jet cascade by P_i and neglecting other than u, d or s - flavor, we get (1) by isospin symmetry $p_u=p_d\equiv p$ and (2) by probability conservation $2p+p_s=1$.

Quantum number retention can be formulated for any additive quark quantum number, N_Q, as $\langle N\rangle=N_Q-L_N$ where L_N is the leakage factor

corresponding to an average quark flavor. The leakage can be expressed as $L_N = \alpha\Sigma_i p_i N_i + (1-\alpha)\Sigma_{ij} p_i p_j N_{ij}$ where α gives the relative amount of mesons at the jet selection point y^*_o.

Baryons (i.e., $\bar{q}\bar{q}$-pairs in Figure 22) contribute if they are produced at $y^* \simeq y_o$, only. As an example, 15% of protons relative to all positively charged hadrons at $y^* = y_o$ leads to about 5% decrease in the leakage factor in the case of the jet net charge. In the following, we will neglect baryon production.

For jet isospin, I then obtain, $\langle I_z \rangle = I_Q - L_I = I_Q - \Sigma_i p_i I_i = I_Q$ (absolutely retained). For the jet strangeness, $\langle S \rangle = S_Q - L_S = S_Q + P_s = P_s$ for u- and d-jets and $\langle S \rangle = -(1-P_s)$ for s-jets. For the jet net charge, I find, $\langle Q \rangle = Q_Q - L_Q = Q_Q - \Sigma_i p_i Q_i = 1-p$ for u-jets and $\langle Q \rangle = -p$ for d- and s-jets.

Figure 23 shows the expected net charge distribution $\frac{1}{N_{ev}} \frac{d(N^+-N^-)}{dY^*}$ for the reactions $\bar{\nu}_\mu p \to \mu^+ X^o$ and $\bar{\nu}_\mu n \to \mu^+ X^-$ in different W-regions. At finite c.m.s energies, the overlap between the target and current fragmentation regions prevents the measurement of the absolute net jet charge. Figure 24 shows the expected net charge distribution for the antineutrino interactions off an isoscalar target. In Figure 25, the experimental results for the net charge from an $\bar{\nu}N$ experiment in the Fermilab 15-foot bubble chamber are shown.[15] Qualitative agreement with expectation is observed. Presence of the hole fragmentation region in the negative y*-region may complicate the situation in the backward c.m.s. hemisphere.

Assuming that short range correlations dominate in the central rapidity region, we will parametrize the net charge distribution in the form $\frac{1}{N_{ev}} \frac{d(N^+-N^-)}{dy^*} = C\exp(\lambda|y^*-y^*_{max}|)$ where $1/\lambda$ is the correlation

length. The maximum rapidity interval $\Delta y^*_{max} \propto \ln W^2$, i.e., the net charge lost under the overlap will be proportional to $W^{-2\lambda}$. We have checked this relationship by plotting $\ln\langle Q\rangle$ versus $\ln W$ and obtained $\lambda = 0.5\pm0.1$.

Figure 26 shows the average net charge of the hadrons forward in the c.m.s.plotted as a function of W^{-1}. An extrapolation of these results to $W\to\infty$ gives for the "overlap free" jet net charge $\langle Q\rangle = -(0.44\pm0.09)$ in $\bar{\nu}N$ CC interactions and $\langle Q\rangle = 0.54\pm0.12$ is νN CC interactions.[15] From these measurements, I then obtain $p = 0.44\pm0.09$ ($\bar{\nu}N$-results), $Ps/p\sim0.27$ and $\langle S\rangle = Ps = 0.12$. These results are consistent with the results obtained from the measurement of the $\overset{(-)}{K}{}^0/h^-$-ratio in the antineutrino induced jets in the same experiment.

Weighted Charge. Field and Feynman have proposed an alternative way of distinguishing quark jets of different flavor.[12] In this approach, one weights each particle with a z-dependent weight such that particles closer to the overlap region get a small weight and particles with large fractional energy z (further from the overlap region) get a large weight, i.e., the weighted charge is defined as $Q_W^{\nu,\bar{\nu}}=\Sigma_i(z_i)^r e_i$, where r is a small number and e_i is the integer charge of the ith hadron in the final state. Resulting distributions from an $\bar{\nu}N(\nu N)$ experiment in the Fermilab 15-foot bubble chamber are shown in Figure 27 (Fig. 28) for antineutrino (neutrino) charged current events.[15] To compare with the predictions which are calculated for 10 GeV quark jets, we select c.m.s. energies above 6 GeV. Corresponding predictions by Field and Feynman are shown for the d- and u-quark jets with the two values of r, r=0.2, and r=0.5.

x-dependence of the Jet Net Charge. In terms of the QPM, any x-dependence of the jet net charge, or the average weighted charge, at

fixed c.m.s.energy, would reflect contributions from the $\bar{u}$-jets in $\bar{\nu}N$ CC interactions. In Figure 29, I present the average weighted charge (r=0.5) with the selection W>4 GeV as a function of x.[15] Using the ocean quark distribution obtained from the same experiment, I have calculated the predicted x-dependence of the average weighted charge using the average weighted charge values of -0.15, and -0.26 for the d-quark and $\bar{u}$-quark jets, respectively. I then correct these predictions for the overlap between the target and current fragmentation regions by using the charge extrapolation result and the kinematical relation between x, Q^2,W^2 ($W^2 = Q^2(1/x-1)+M^2$), and obtain the qualitative agreement with the data (Fig. 29).

3.4 Fragmentation Functions - "QCD Tests"

The next to the leading order calculations by N. Sakai using QCD perturbation theory indicate a presence of a factorization violation in the inclusive cross section for the processes $lN \to lhX$. The double moments

$$\int dx\, x^n \int dz z^m\, \sigma(x,z,Q^2) = A_{nm}\, (\ln Q^2)^{-\gamma_n}\, (\ln Q^2)^{-\gamma_m}\, (1+\frac{F_{nm}}{\ln Q^2})$$

where $\gamma_{n,m}$ are the anomalous dimensions, do not factorize in their dependences on n and m, but there is a term $F_{nm}/\ln Q^2$ which violates the factorization hypothesis.

In testing the predicted non-factorization or Q^2-dependence of the fragmentation functions, one should note, however, the following: (1) At low c.m.s.energies there are contributions from the overlap, quasi-elastic channels, etc., which intimately depend on x and Q^2; (2) Non-singlet combinations of the fragmentation functions $D^{ns}(z)=D^{h+}(z)-D^{h-}(z)$ are related to the jet net charge $\langle Q\rangle=\Sigma_h\, e_n \int dz\, (D^{h+}(z)-D^{h-}(z))$ and are expected to depend on x and Q^2 due to the ocean quark contributions at low x.

3.5 Transverse Structure of the Jets

A constituent bound into the nucleon dimensions should, by the Uncertainty Principle, have "primordial" motion. The parton, with initial transverse momentum k_T, would retain that additional degree of freedom in the pointlike interaction with the current. The observed final state hadrons would then receive two kinds of contributions to their total transverse momentum, P_T, relative to the direction of the initial quark, $\langle P_T^2 \rangle = z^2 \langle k_T^2 \rangle + \langle h_T^2 \rangle$, where h_T is the net transverse momentum gained in the fragmentation.

The primary source of uncertainty in the studies of transverse spectra of jets is the determination of the direction of the initial quark, the jet axis. A quantity independent of experimental uncertainties is the transverse momentum of the hadrons measured relative to the lepton production plane, P_{out}. Assuming azimuthal symmetry in the hadron production, there is a simple relation between P_{out} and P_T: $\langle P_{out}^2 \rangle = \frac{1}{2} \langle P_T^2 \rangle$.

Figure 30 shows the average angle between the two popular jet axes, the thrust axis and the sphericity axis, plotted as a function of the c.m.s energy, W. Only above 10 GeV c.m.s energy does the jet axis become reasonably well defined (within 10 degrees). Figure 30 also includes, for comparison, data from an $\bar{\nu}p$ experiment and from an e^+e^--experiment.[16]

In Figure 31, $\langle P_T^2 \rangle$ and $\langle P_{out}^2 \rangle$ are plotted as functions of W. $\langle P_T^2 \rangle$ is measured relative to the thrust axis.[16] Solid lines represent LPS predictions. Good agreement with the e^+e^- data and with the LPS predictions is observed.

A quantity relatively free of the uncertainties related to the precise knowledge of the jet axis is the angular energy flow, i.e., into

a given angular cone, $d\lambda$. Figure 32 shows the angular energy flow as a function of the angle, λ in three separate experiments.[16] Support for the universality of the jets in $\bar{\nu}N$ and in e^+e^- interactions is obtained. Figure 33 shows the average opening angle λ as a function of thrust for the three experiments.[16] It would appear that around T=0.8 that one can speak about a jet as a geometrical entity ($\langle\lambda\rangle \sim 30^0$).

3.6 Conclusions

In agreement with the quark fragmentation picture, we have found evidence for d-quark jets (u-quark jets) in antineutrino (neutrino) charged current interactions. The probability of finding a u- or d-quark in the quark jet cascade was measured to be 0.44±0.05. No significant x-dependence was seen in the single-particle distributions in the antineutrino induced jets.

Longitudinal and transverse structure of the quark jets was seen to follow the predictions of the simple QPM. No need for perturbative QCD corrections to the QPM predictions was required.

Acknowledgements.

I want to thank the Organizers of the Arctic School of Physics for the unique Summer School with the hard-working participants and inspiring atmosphere. Numerous discussions and collaboration with the members of the Fermilab experiment E-180 are gratefully acknowledged. I would also like to express appreciation to Kenneth Lassila for carefully reading the manuscript and making several useful suggestions.

REFERENCES

1. Feynman, R.P., Photon-Hadron Interactions, (W. A. Benjamin, New York, 1972). For a recent review see: Buras, A. J., Review of Modern Physics, vol. 52, 1 (1980).
2. Ammosov, V. V., et al, Inclusive Charged-Current Antineutrino-Nucleon Interactions at High Energy, to be published (preliminary data).
3. Bosetti, P., et al, Nucl. Phys. B142, 1 (1978). P. Allen et al, Single π^+ Production in CC νN_2 Interactions, CERN/EP 80-69 (1980), submitted to NPB.
4. Atwood, W. B., Lepton-Nucleon Scattering, lectures at the SLAC Summer Institute on Particle Physics, Stanford, California, July 9-20 (1979), SLAC-PUB-2428 (1979).
5. Heagy, S. M., Charged Current Neutrino and Antineutrino Interactions and Nucleon Structure Functions, A Ph.D. Thesis at the University of Wisconsin-Madison (1980).
6. Mestayer, M., SLAC Report No. 214.
7. Gordon, B. A., et al, Phys. Rev. Lett. 41, 675 (1978).
8. Turlay, R., Experimental Review of High Energy Neutrino Physics, Academic Training Lectures at CERN (1979).
   Knobloch, J., The Structure and the Amount of the Sea, Contribution to the 1980 Rochester Conference in Madison, Wisconsin-Madison (1980).
   de Groot, J. G. V. et al, Z, Physik C, Particles and Fields 1, 143-162 (1979).
9. Clark, A. R., et al, Measurement of the Charm Structure Function and Its Role in Scale-Noninvariance, Fermilab-Pub-80/41 (1980).

REFERENCES (cont.)

10. Altarelli, G. and Parisi, G.,Nucl. Phys. B126, 198 (1977). See also: L. F. Abbot and R. M. Barnett, The Effect of $1/Q^2$ and α_s Corrections on Tests of QCD, SLAC-PUB-2325 (1979).

11. Bjorken, J. D., Hadron Final States in Deep-Inelastic Processes, International Summer Institute on Theoretical Particle Physics 7th, Hamburg (1975) p. 93, and references cited therein.

12. Field, R. D. and Feynman, R. P., Nucl. Phys. B136, 1 (1978).

13. Ammosov, V. V., et al, Quark Jets from Antineutrino Interactions II; Inclusive Particle Spectra and Multiplicities in the Quark Jets, to be published (preliminary data).

14. Ammosov, V. V., et al, Phys. Lett. 93B, 210 (1980).

15. Nezrick, F., Neutrino-79 Conference, Bergen, Norway (1979).
Berge, J. P., et al, Phys. Lett. 91B, 311 (1980).
Berge, J. P., et al, Quark Jets from Antineutrino Interactions I; Net Charge and Factorization in the Quark Jets, Fermilab-Pub-80/62-EXP (1980).

16. Efremenko, V. I., et al, Quark Jets from Antineutrino Interactions III; Transverse Structure of the Quark Jets, to be published (preliminary data).

17. McPharlin, T. P., et al, Phys. Lett. 90B, 479 (1980).

18. Zichichi, A., Split Field Magnet Data from the CERN ISR, private communication (1980).

19. Berger, Ch., et al, Phys. Lett. 78B, 176 (1978).

Table I. Characteristics of an "average" bubble chamber experiment and of an "average" electronic counter experiment.

Quantity	Bubble Chamber	Electronic Detector
$\Delta P_L/P_L$	5% *	5% *
$\Delta\theta_L$	1 mrad *	1 mrad *
$\Delta E_H/E_H$	15% *	10% *
min P_L	5 GeV	10 GeV
min E_H	1 GeV	10 GeV
$\Delta\Omega/4\pi$	1	10^{-3} - 1
Efficiency	95%	70-95%

* For 100 GeV P_L or E_H

Table II. Experimental results on $I_3 = \int_{x_{min}}^{1} F_3(x)\,dx$

Group	x_{min}	I_3
CDHS[8]	0.005	2.7 ± 0.3
BEBC[3]	0.02	2.94 ± 0.56
	0.06	2.33 ± 0.16
	0.10	2.01 ± 0.15
HPWFRO[5]	0.005	2.6 ± 0.5*

* Correction for Δ^{eN} in the valence quark distribution is accounted for.

Table III. Experimental results for $I_3=\int xF_3 dx, I_2=\int F_2 dx$ with $Q^2>2$ GeV^2.

Group	$I_2^{\nu N}$	$I_3^{\nu N}$
BEBC[3]	0.51 ± 0.05	0.40 ± 0.08
CDHS[8]	0.44 ± 0.02	0.31 ± 0.03

Table IV. Experimental results for the fraction of anti-quarks in the nucleon.

Group	$\bar{Q}/Q$	$\bar{S}/Q$	$\bar{S}/\bar{Q}$
HFWFRO[5]	0.13 ± 0.04	0.03 ± 0.01	0.23 ± 0.10
CDHS[8]	0.14 ± 0.01	0.03 ± 0.01	0.21 ± 0.07

Table V. Contribution of the "diffractive" $c\bar{c}$-production into the total $F_2^{\mu N}$.

ν(GeV)	27	42	67	106	168	
Q^2 $(GeV/c)^2$	$\frac{10^4 \partial F_2(c\bar{c})/\partial \ell n Q^2}{10^4 \partial F_2(\mu N)/\partial \ell n Q^2}$					x_B
0.63	17	30	43	54	58	
	1070	1090	1110	1120	1130	
1.0	23	43	63	77	84	
	980	1010	1040	1050	1060	0.002
1.6	30	59	87	107	116	
	650	680	700	720	730	0.003
2.5	36	73	110	139	146	
	310	340	350	360	360	0.005
4.0	36	80	128	162	163	
	320	390	430	460	480	0.008
6.3	29	75	128	165	154	
	210	330	410	460	490	0.013
10	15	54	104	138	112	
	50	220	340	430	480	0.020
16	4	27	64	90	52	
	-130	50	230	360	440	0.032
25	-2	7	26	40	0	
	-189	-126	50	230	370	0.050
40	0	-1	6	10	-22	
	-31	-171	-122	50	240	0.080
63		0	1	1	-16	
		-23	-154	-119	50	0.130

FIGURE CAPTIONS

1. Schematic illustration of (a) a deeply inelastic lepton-nucleon interaction and (b) a subsequent fragmentation of the struck quark.
2. Structure function $F_2(x)$ as a function of Q^2 with $0.2 < x < 0.3$ from an $\bar{\nu}N$-experiment (Ref. 2).
3. Structure function F_2 measured in an $\bar{\nu}N$-experiment (Ref. 2), in a νN-experiment (Ref. 9) and in an eN-experiment (Ref. 4). F_2^{eN} is multiplied by 18/5 (data points) and a fit to the eN data points by 2 (dashed line).
4. Integral $n_v = \int_{x_{min}}^{1} F_3(x)dx$ as a function of x_{min} (Ref. 8). Dashed line represents a fit to xF_3 at all x.
5. Valence quark distribution $xV(x) = \frac{1}{2}(xF_3^{\nu} + F_3^{\bar{\nu}})$ (Ref. 5).
6. (a) $F_2^{\nu,\bar{\nu}}$ as a function of Q^2 (Ref. 2,3) for $0.01 < x < 0.10$ and $0.6 < x < 1.0$, and (b) xF_3^{ν} as a function of Q^2 and x (Ref. 8).
7. Kinematically allowed regions (a) for the Fermilab $\bar{\nu}N$ 15-foot bubble chamber experiments (Ref. 2), (b) for the CDHS-experiments at CERN (Ref. 8) and (c) for the SLAC eN experiment (Ref. 4).
8. De-smearing function $\varepsilon(x) = G^{true}(x)/G^{smeared}(x)$ as determined in the Fermilab $\bar{\nu}N$ experiment (Ref. 2). Percentages indicate amount of smearing.
9. $xO(x) \sim F_2^{\nu} - xF_3^{\nu}$ as a function of x and Q^2 (Ref. 8).
10. $F_2^{en}-F_2^{ep}$ for inelastic eN-scattering together with the data for elastic ep cross section (Ref. 4).
11. Energy dependence of the cross section $\sigma(\nu p \to \mu^- \Delta^{++})$ (Ref. 3).
12. Q^2-dependence of the cross section $\sigma(\nu p \to \mu^- \Delta^{++})$ (Ref. 3).
13. Kinematically allowed region for the diffractive process $\nu p \to \mu^- p\rho^o$.

FIGURE CAPTIONS (cont.)

14. Determination of Λ by plotting $M^{-1/dn}$ versus Q^2 (Ref. 8) and fitting straight lines through the data points.
15. log M^{ns} (n,Q^2) versus log M^{ns} (n',Q^2) for the eN-data (Ref. 4). Straight lines are leading order QCD predictions.
16. Rapidity distribution resulting from the parton fragmentation in deeply inelastic lepton-nucleon scattering (Ref. 11).
17. $R=D_p^h(z,Q_o^2,x_i)/D_p^h(Z,Q_o^2,x_j)$ with (a) $0.01<x_1<0.20$, $0.1<x_2<0.3$, (b) $0.01<x_1<0.2$, $x_2>0.2$, and (c) $0.1<x_i<0.3$, $x_2>0.2$. The selection in Q^2 is for a, b and c: $3<Q^2<10$ GeV$^2/c^2$ (Ref. 15).
18. Fragmentation functions $(1/N_{ev})(dN^{\pm}/dz)$ for $\bar{\nu}$ CC induced jets (Ref. 2), ep-experiment (Ref.17), e^+e^--annihilation (Ref.17), pp-experiment (Ref.18) and $(1/N_{ev})dN^o/dz$ for the ep-experiment
19. Fragmentation functions $(1/N_{ev})/dN^+/dz)$ for $\bar{\nu}$ CC induced jets (Ref. 2, corrected for proton contamination), for $\bar{\nu}$ CC induced jets (<u>not</u> corrected for proton contamination) and $(1/N_{ev})(dN^-/dz)$ for $\bar{\nu}$ CC induced jets (Ref. 2), for νCC induced jets.
20. Ratio $h^-/h^+ = D^{h-}(z)/D^{h+}(z)$ as a function of $z - E_h/\nu$ for $\bar{\nu}$ CC induced jets (Ref. 2).
21. Ratio $K^o/h^- = \int_{z_{min}}^{1} dz(D^{K^o}(z)/D^{h^-}(z))$ as a function of z_{min} for $\bar{\nu}$ CC induced jets (Ref. 2).
22. Schematic illustration of the origin of the quantum number leakage in (a) meson production and in (b) baryon production. The dashed line represents a physical selection of the current fragments.
23. Expected rapidity distribution of the net charge $(1/N_{ev})(dN^+-dN^-)/dy^*$ in (a) $\bar{\nu}$p-interactions and (b) $\bar{\nu}$n-interactions.

FIGURE CAPTIONS (cont.)

24. Predicted rapidity distribution of the net charge $(1/N_{ev})(dN^{+}-dN^{-})/dy^{*}$ in $\bar{\nu}N$ interactions off an isoscalar target.
25. Net charge of hadrons produced in $\bar{\nu}N$ CC interactions as a function of the c.m.s rapidity in three different W-intervals: $3<W<4$ GeV, $4<W<6$ GeV, and $6<W<15$ GeV (Ref. 2).
26. Average net charge of the hadrons traveling forward in the hadronic c.m.s as a function of W^{-1}. The dashed line represents a linear fit to the data points above W>3 GeV. The shaded area is a prediction obtained from a Monte Carlo model which does not include the hypothesis of quark fragmentation (Ref. 2).
27. Weighted charge $Q_{W}^{\bar{\nu}} = \Sigma_i (z_i)^r e_i$ for the $\bar{\nu}$ CC induced hadrons traveling forward in the hadronic c.m.s (a) for r=0.2, and (b) r=0.5. The solid curves represent the Field and Feynman predictions for the hadrons arising from the fragmentation of a u-quark with 10 GeV/c incident momentum and the dashed lines the corresponding predictions for the 10 GeV/c d-quark jets (Ref. 2).
28. Weighted charge $Q_{W}^{\nu} = \Sigma_i (z_i)^r e_i$ for the ν CC induced hadrons traveling forward in the hadronic c.m.s (a) for r=0.2 and (b) for r=0.5. The solid curves represent the Field and Feynman predictions for the 10 GeV/c u-quark jets and the dashed line the corresponding prediction for the 10 GeV/c d-quark jets (Ref. 2).
29. Average weighted charge (r=0.5) of the $\bar{\nu}$ CC induced jets as a function of x. The dashed line represents the prediction described in the text. The solid line represents the prediction corrected for the overlap (Ref. 2).

FIGURE CAPTIONS (cont.)

30. Average angle $\langle(\hat{i}_T, \hat{i}_S)\rangle$ between the thrust and sphericity axes as a function of W for the $\bar{\nu}$ CC induced jets (Ref. 2, preliminary data) and for the e^+e^- jets (Ref. 19).

31. Average transverse momentum $\langle P_T^2\rangle$ relative to the thrust axis and $\langle P_{out}^2\rangle$ relative to the $\mu\nu$-plane as functions of W for the $\bar{\nu}$ CC induced jets (Ref. 2), e^+e^--jets (Ref. 19). The solid lines represent predictions of a Monte Carlo LPS model.

32. Angular energy flow $d\varepsilon/d\lambda$ as a function of λ for the $\bar{\nu}$ CC induced jets (Ref. 2), for e^+e^--jets (Ref. 19) at 9.5 GeV with the selection $T>0.85$.

33. Average jet opening $\langle\lambda\rangle$ as a function of thrust for the $\bar{\nu}$ CC induced jets (Ref. 2), for the e^+e^--jets (Ref. 19).

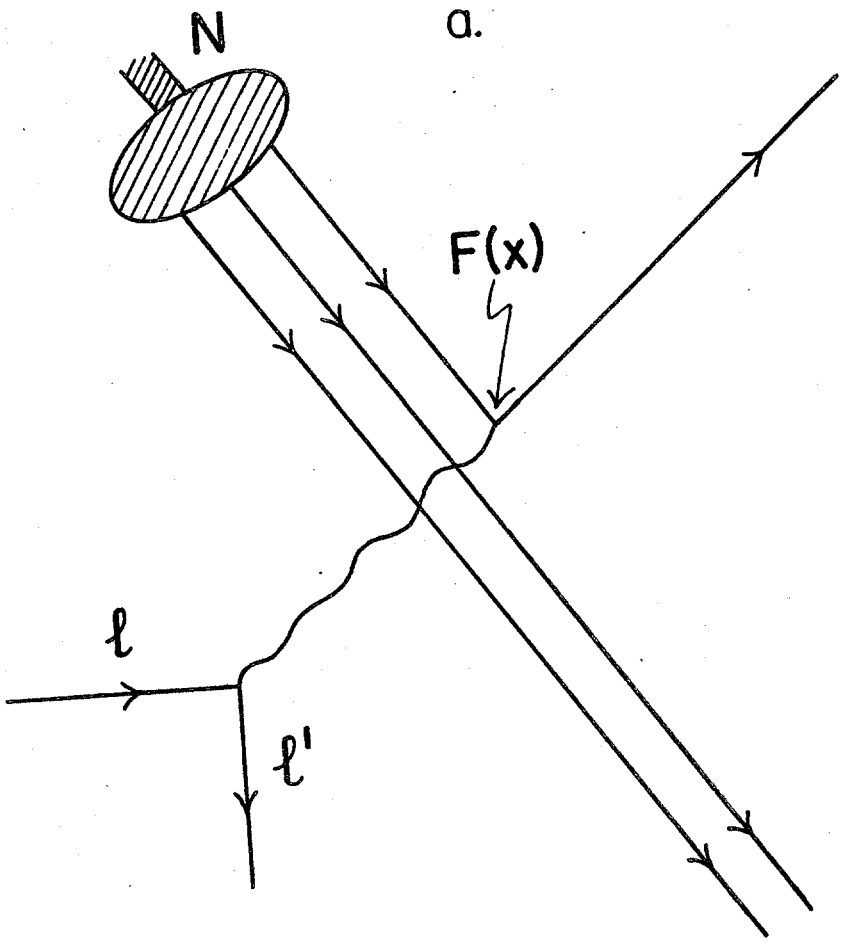

Fig.1

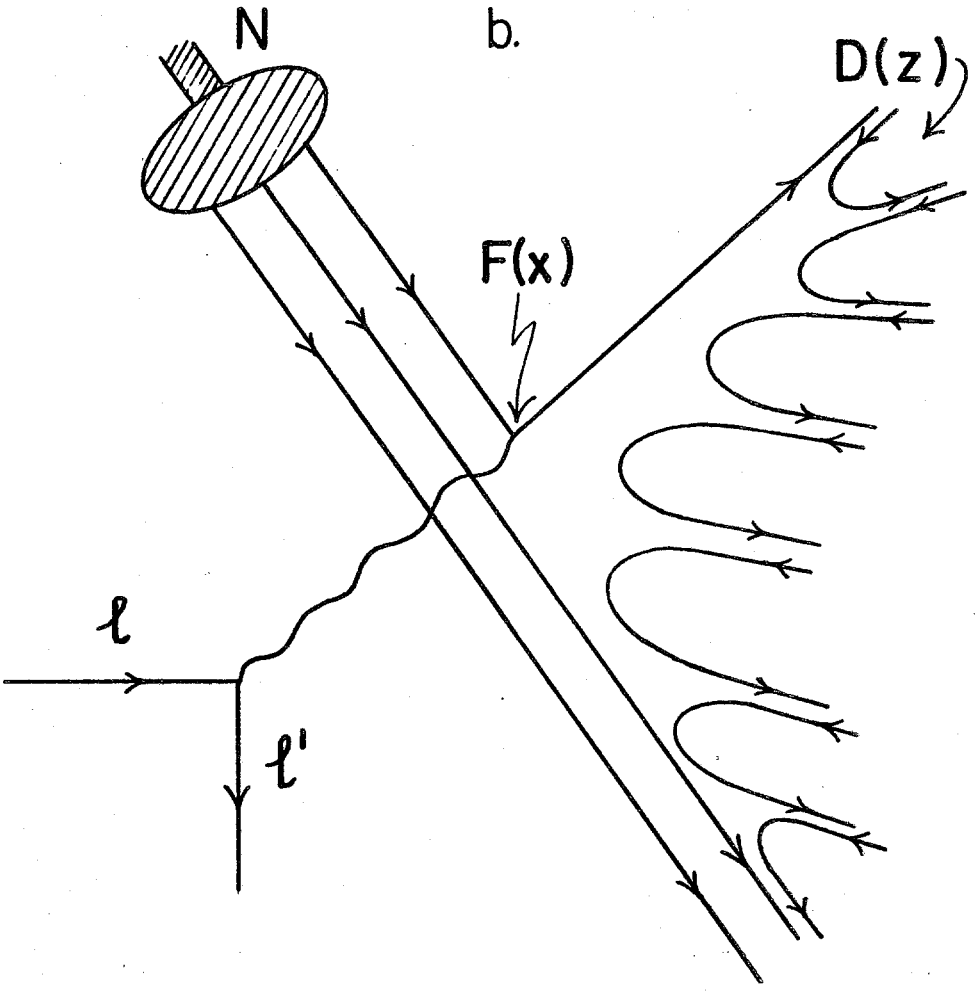

Fig. 1

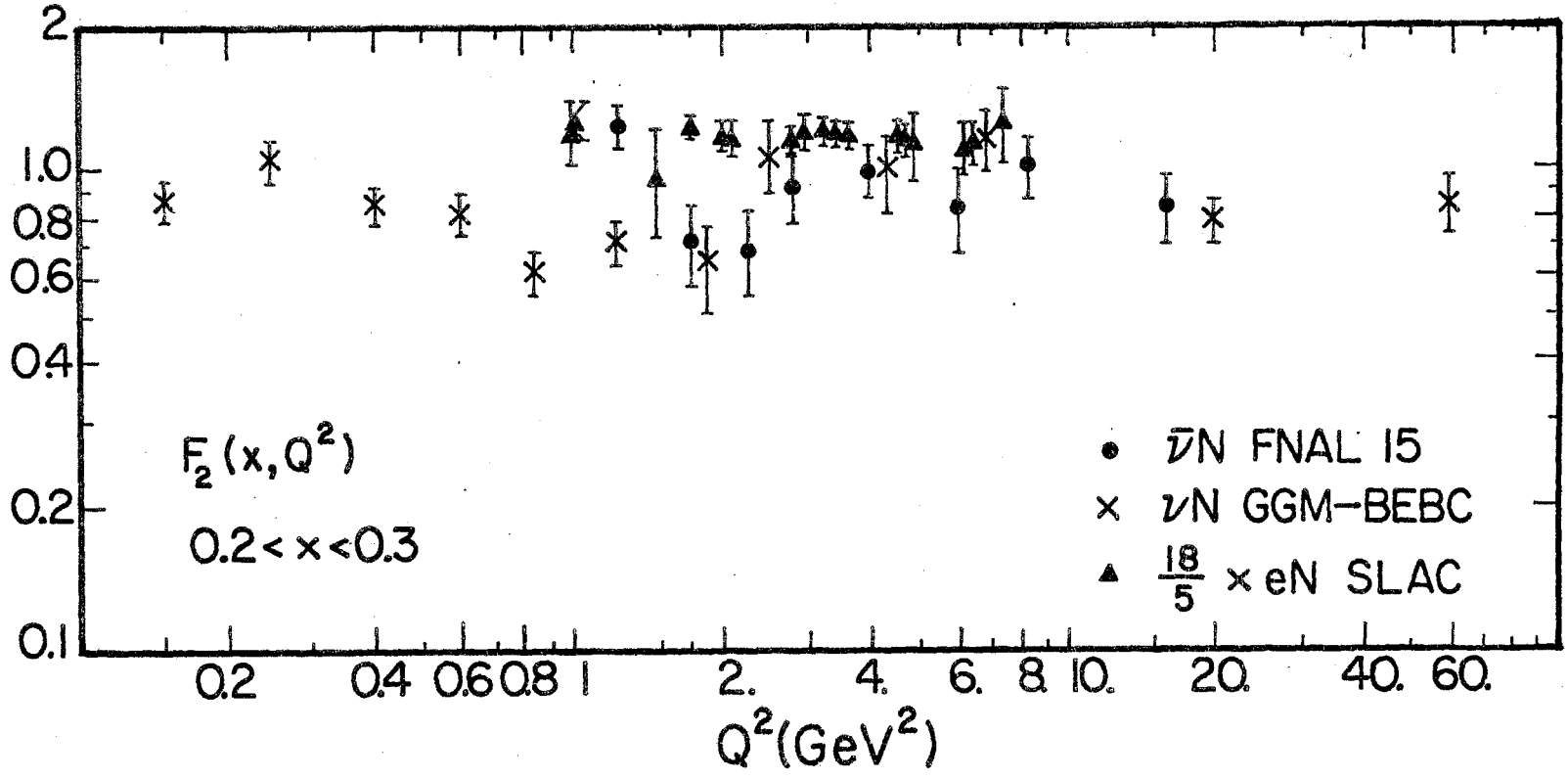
2
1.0
0.8
0.6
0.4
0.2
0.1
$F_2(x,Q^2)$
$0.2<x<0.3$
$\bar{\nu}$N FNAL 15
νN GGM-BEBC
$\frac{18}{5}$ x eN SLAC
0.2
0.4
0.6
0.8
1
2.
4.
6.
8.
10.
20.
40.
60.
$Q^2(GeV^2)$

Fig. 2

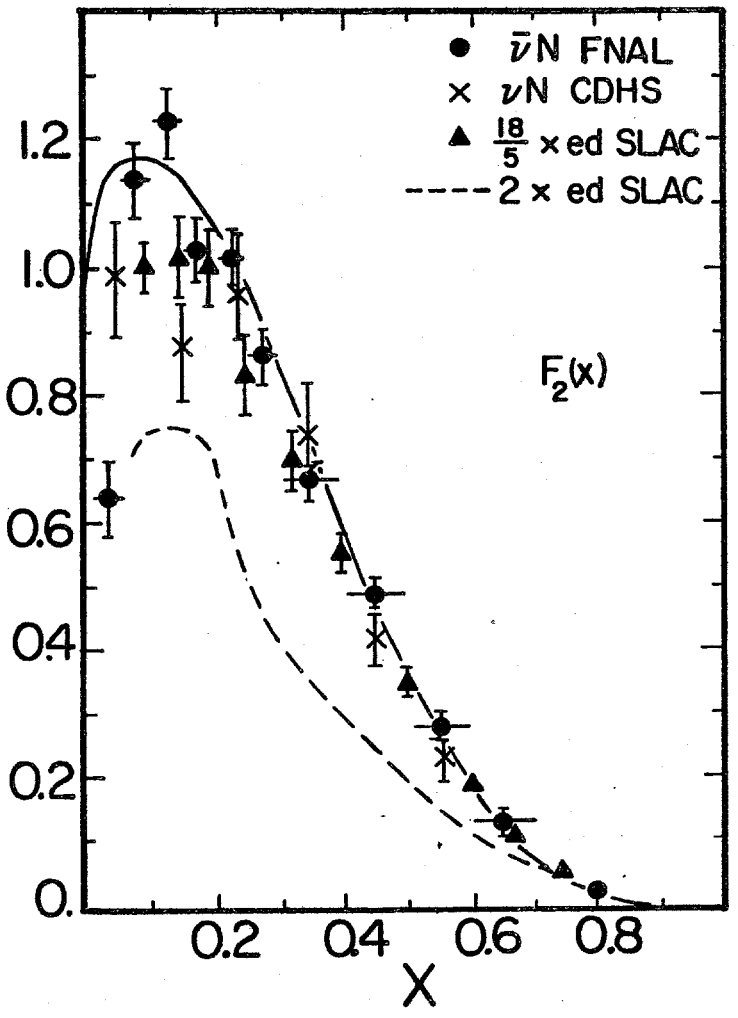
● $\bar{\nu}$N FNAL
× νN CDHS
▲ $\frac{18}{5}$ × ed SLAC
---- 2 × ed SLAC
$F_2(x)$
1.2
1.0
0.8
0.6
0.4
0.2
0.
0.2
0.4
0.6
0.8
X

Fig. 3

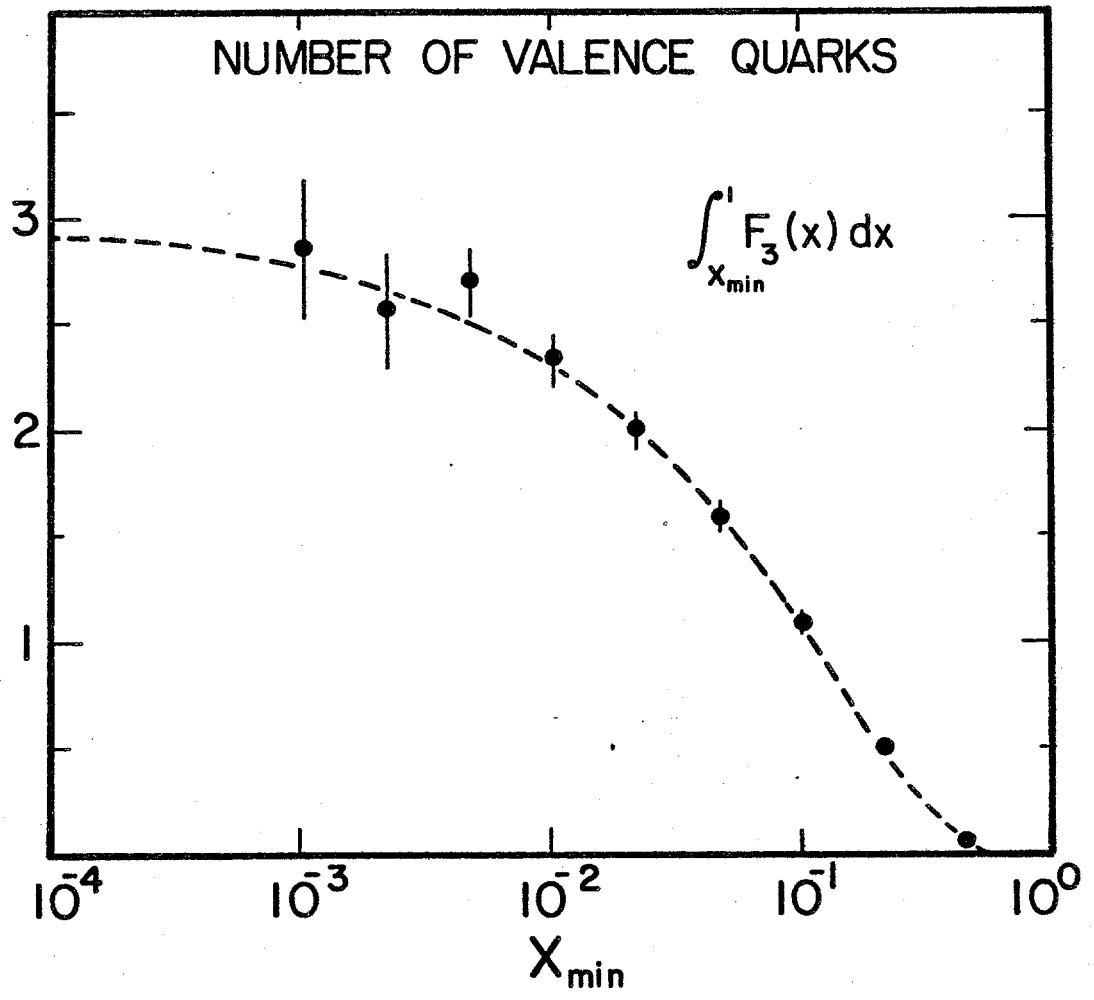
NUMBER OF VALENCE QUARKS
$\int_{x_{min}}^{1} F_3(x)\,dx$
3
2
1
10^{-4}
10^{-3}
10^{-2}
10^{-1}
10^{0}
X_{min}

Fig. 4

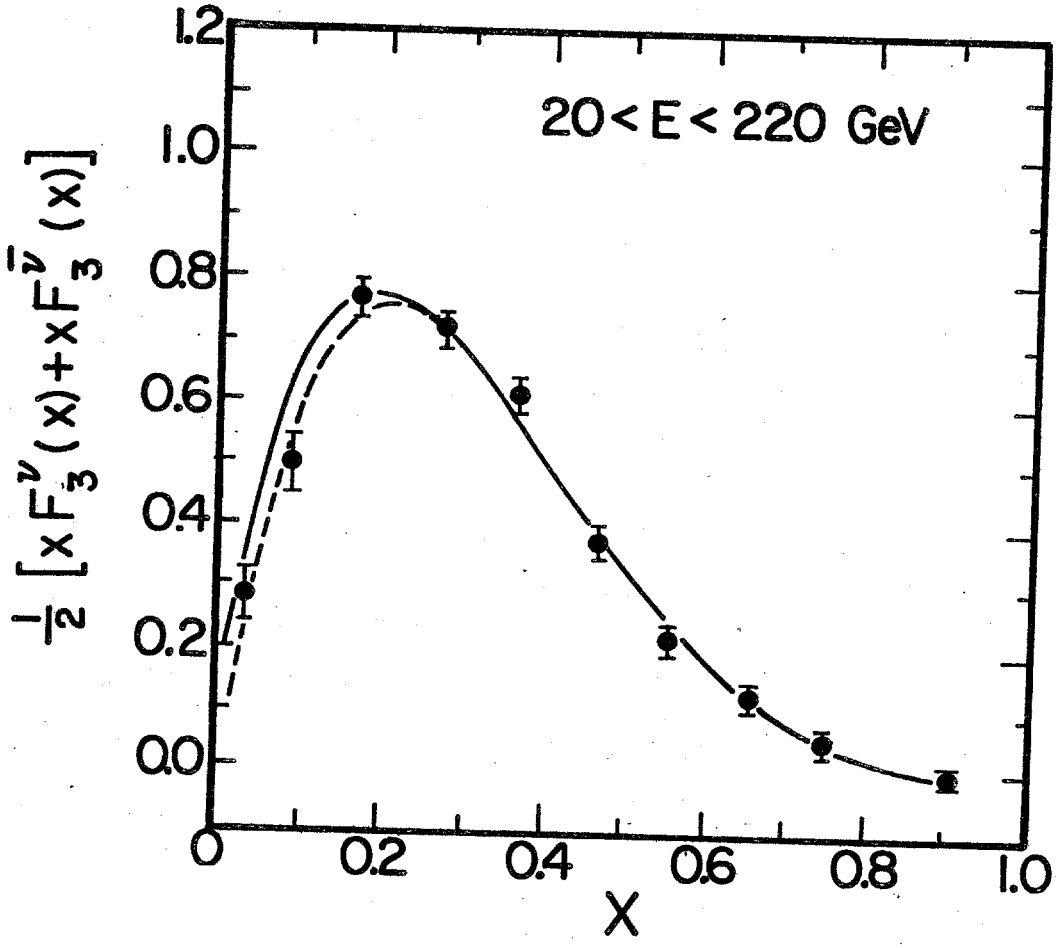

Fig. 5

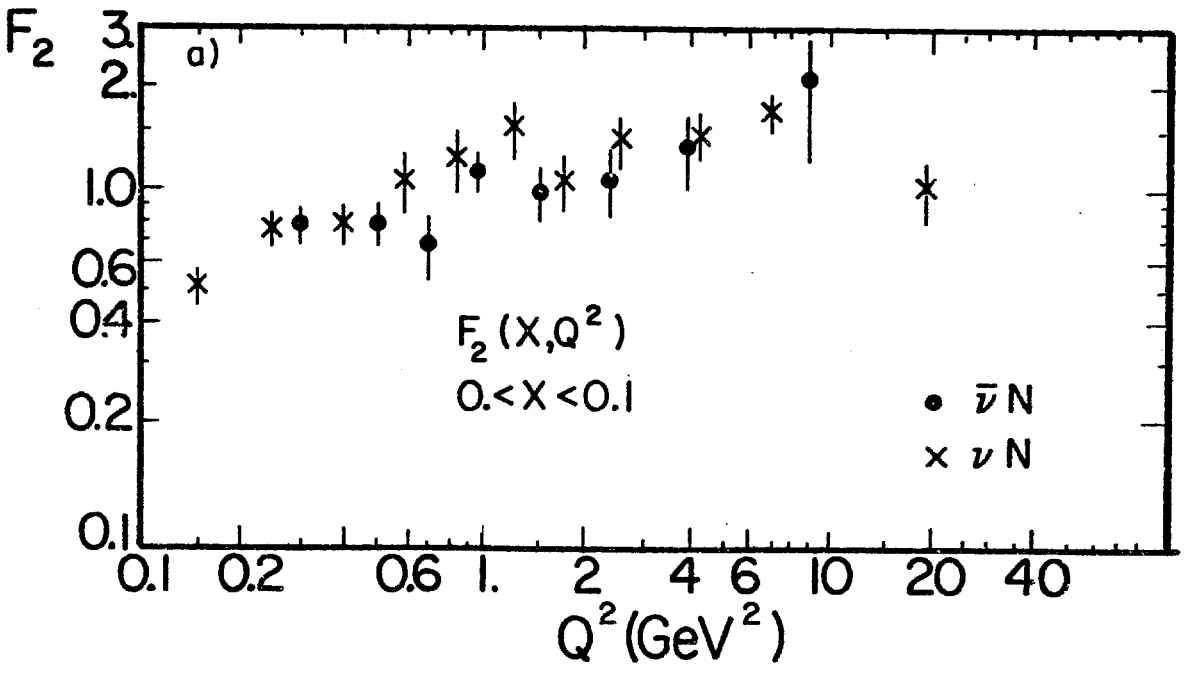

Fig. 6

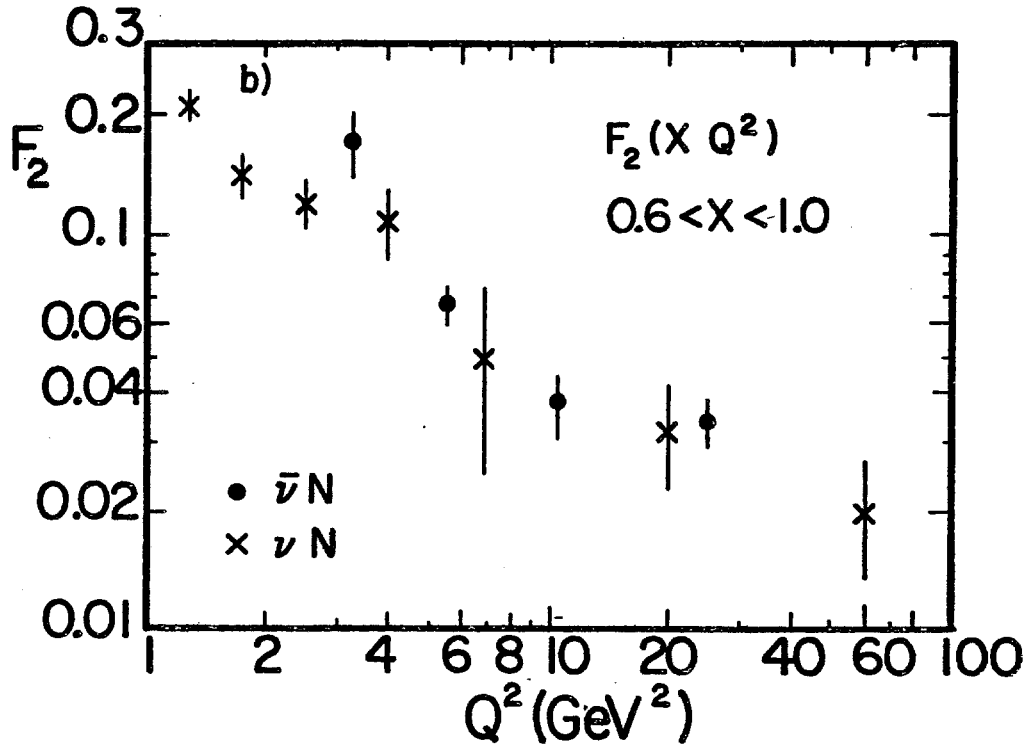

Fig. 6

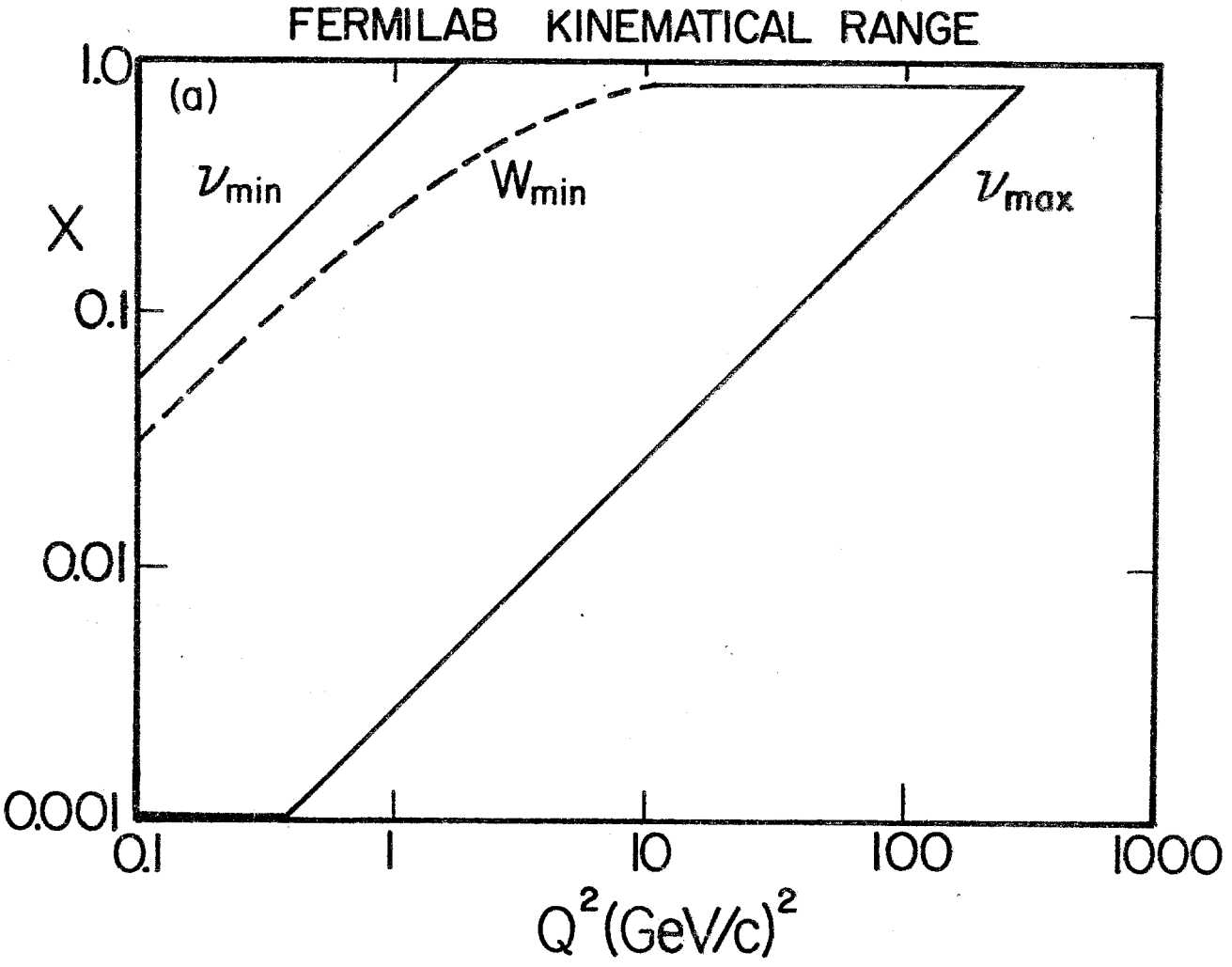
FERMILAB KINEMATICAL RANGE
(a)
ν_{min}
W_{min}
ν_{max}
X
1.0
0.1
0.01
0.001
0.1
1
10
100
1000
Q^2 (GeV/c)^2

Fig. 7

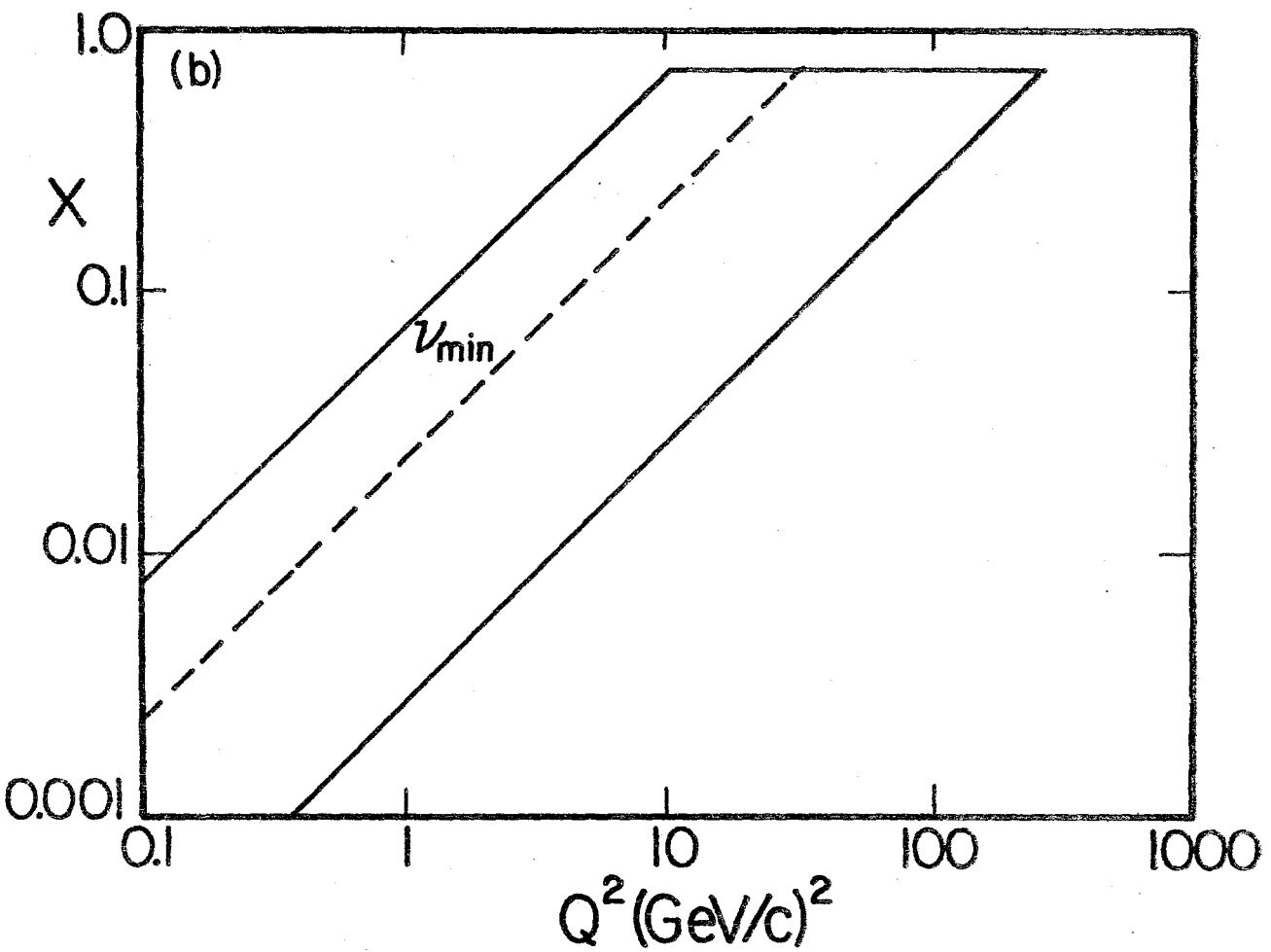
CDHS KINEMATICAL RANGE
(b)
1.0
X
0.1
0.01
0.001
ν_{min}
0.1
1
10
100
1000
Q^2 (GeV/c)^2

Fig. 7

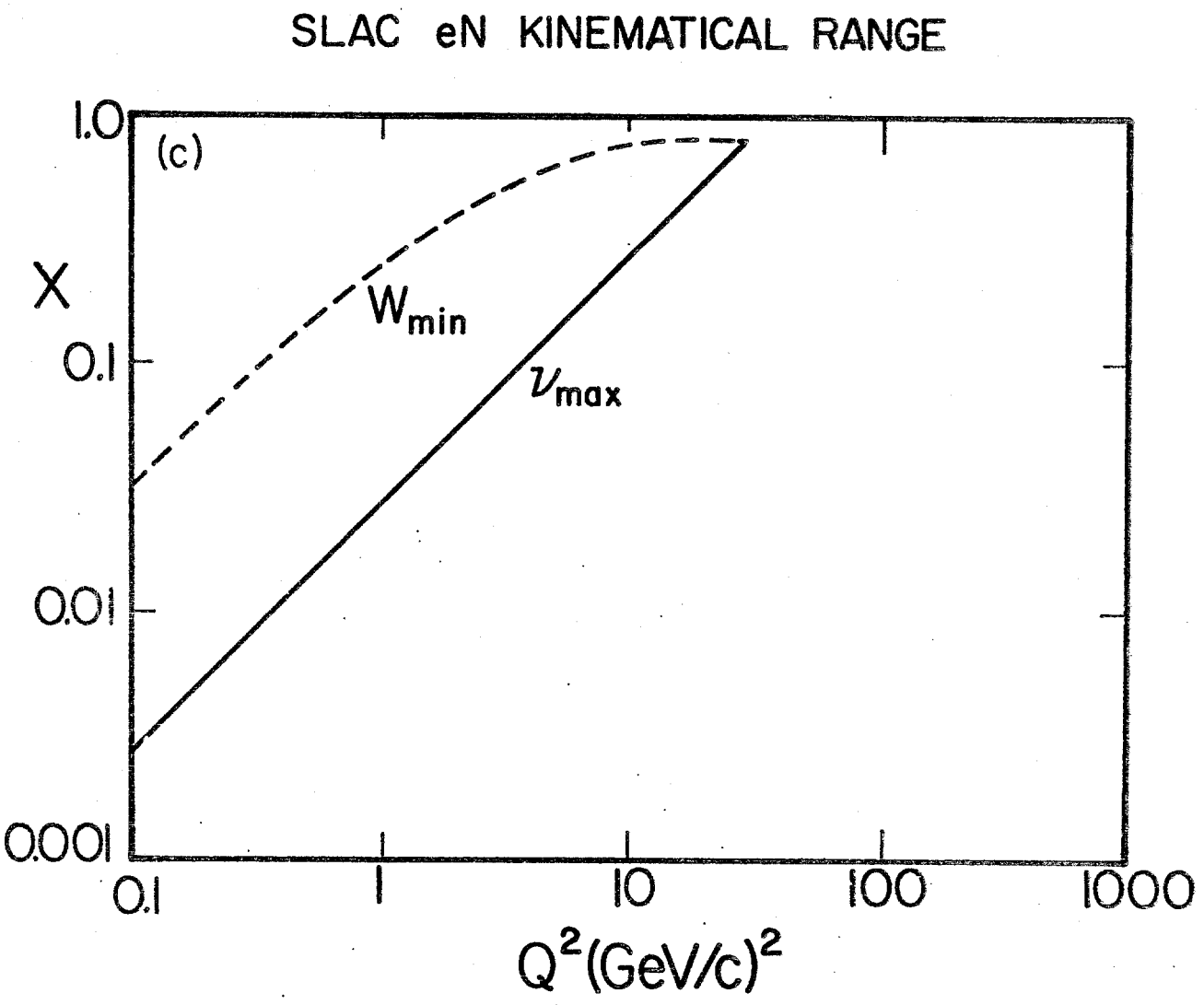
SLAC eN KINEMATICAL RANGE
(c)
X
1.0
0.1
0.01
0.001
W_{min}
ν_{max}
0.1
1
10
100
1000
Q^2(GeV/c)^2

Fig. 7

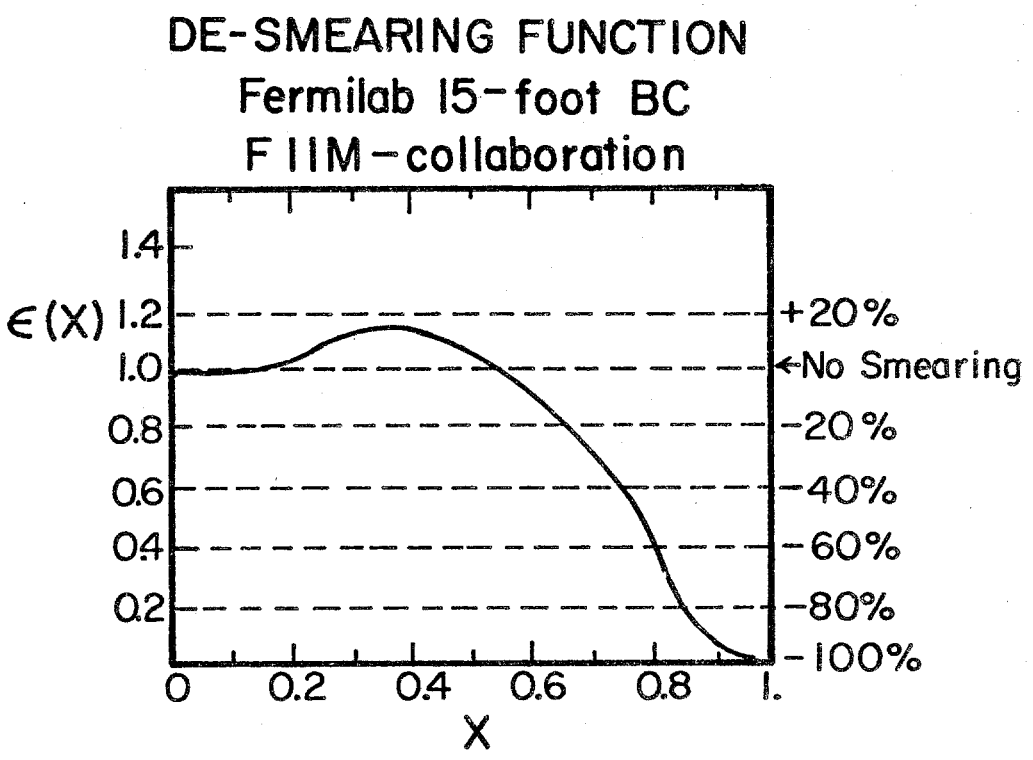
DE-SMEARING FUNCTION
Fermilab 15-foot BC
FIIM-collaboration
ε(X)
1.4
1.2
1.0
0.8
0.6
0.4
0.2
0
0.2
0.4
0.6
0.8
1.
X
+20%
←No Smearing
-20%
-40%
-60%
-80%
-100%

Fig. 8

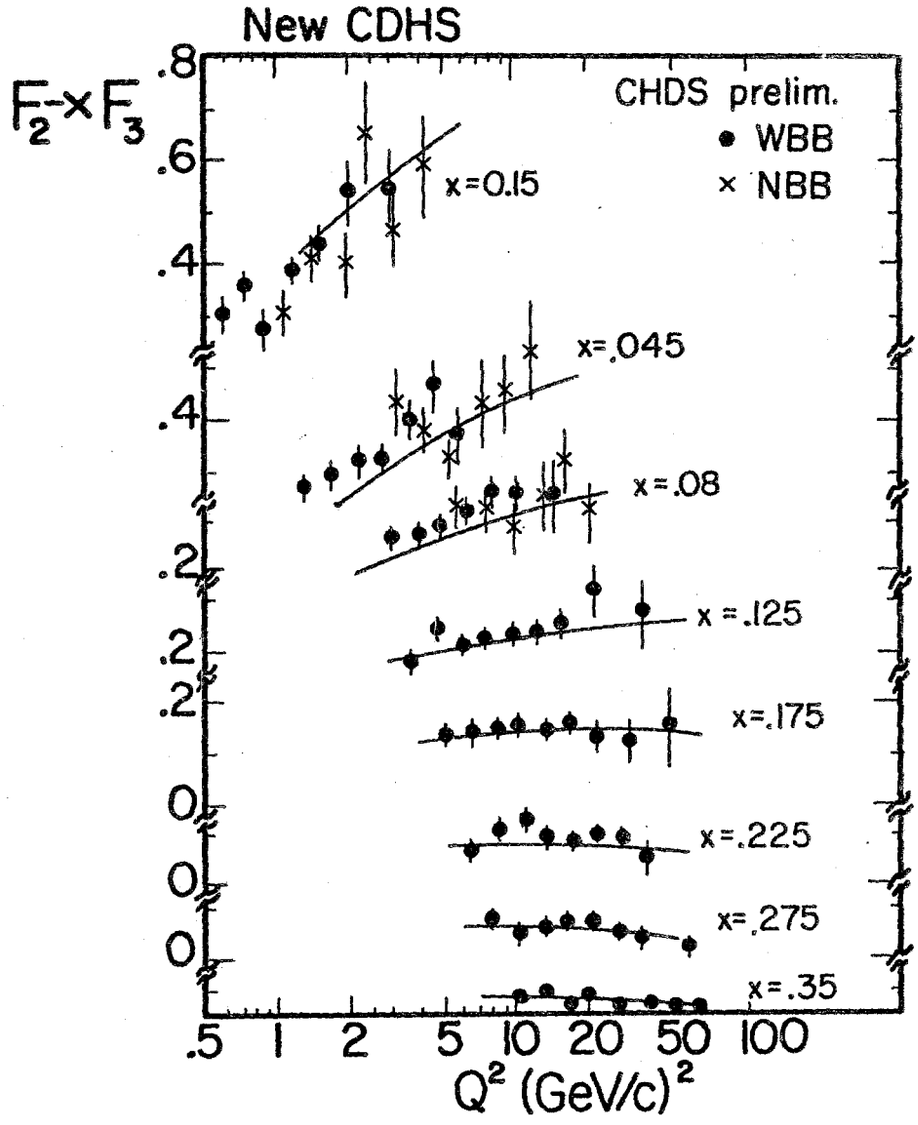
New CDHS
$F_2 - xF_3$
CHDS prelim.
• WBB
× NBB
x=0.15
x=.045
x=.08
x=.125
x=.175
x=.225
x=.275
x=.35
.8
.6
.4
.4
.2
.2
.2
0
0
0
.5
1
2
5
10
20
50
100
Q^2 (GeV/c)^2

Fig. 9

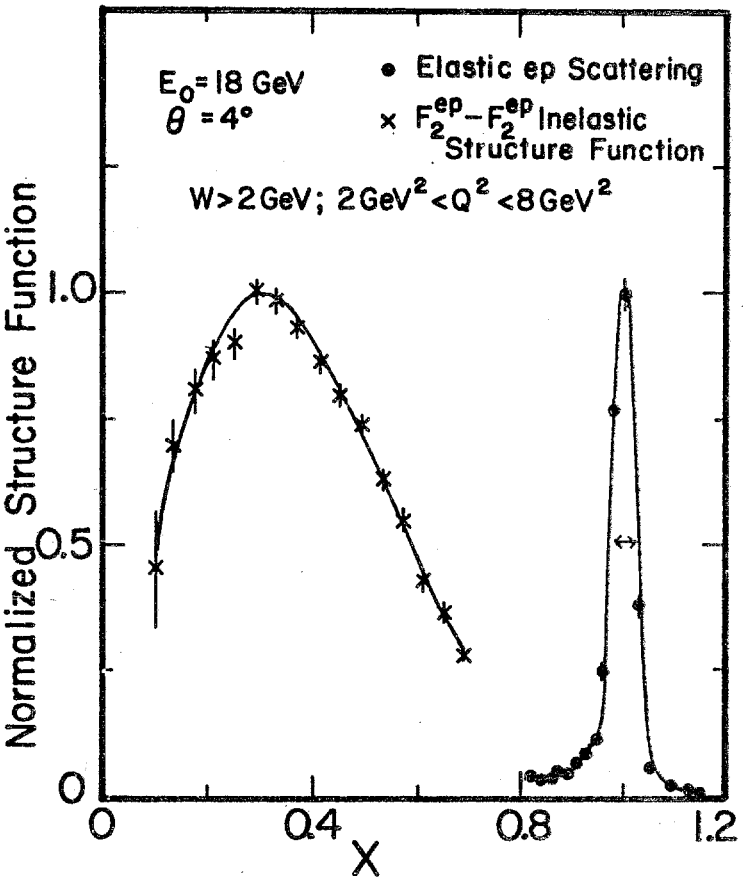
E_0= 18 GeV
θ = 4°
• Elastic ep Scattering
× $F_2^{ep}-F_2^{ep}$ Inelastic Structure Function
W>2GeV; 2GeV^2<Q^2<8GeV^2
Normalized Structure Function
1.0
0.5
0
0
0.4
0.8
1.2
X

Fig. 10

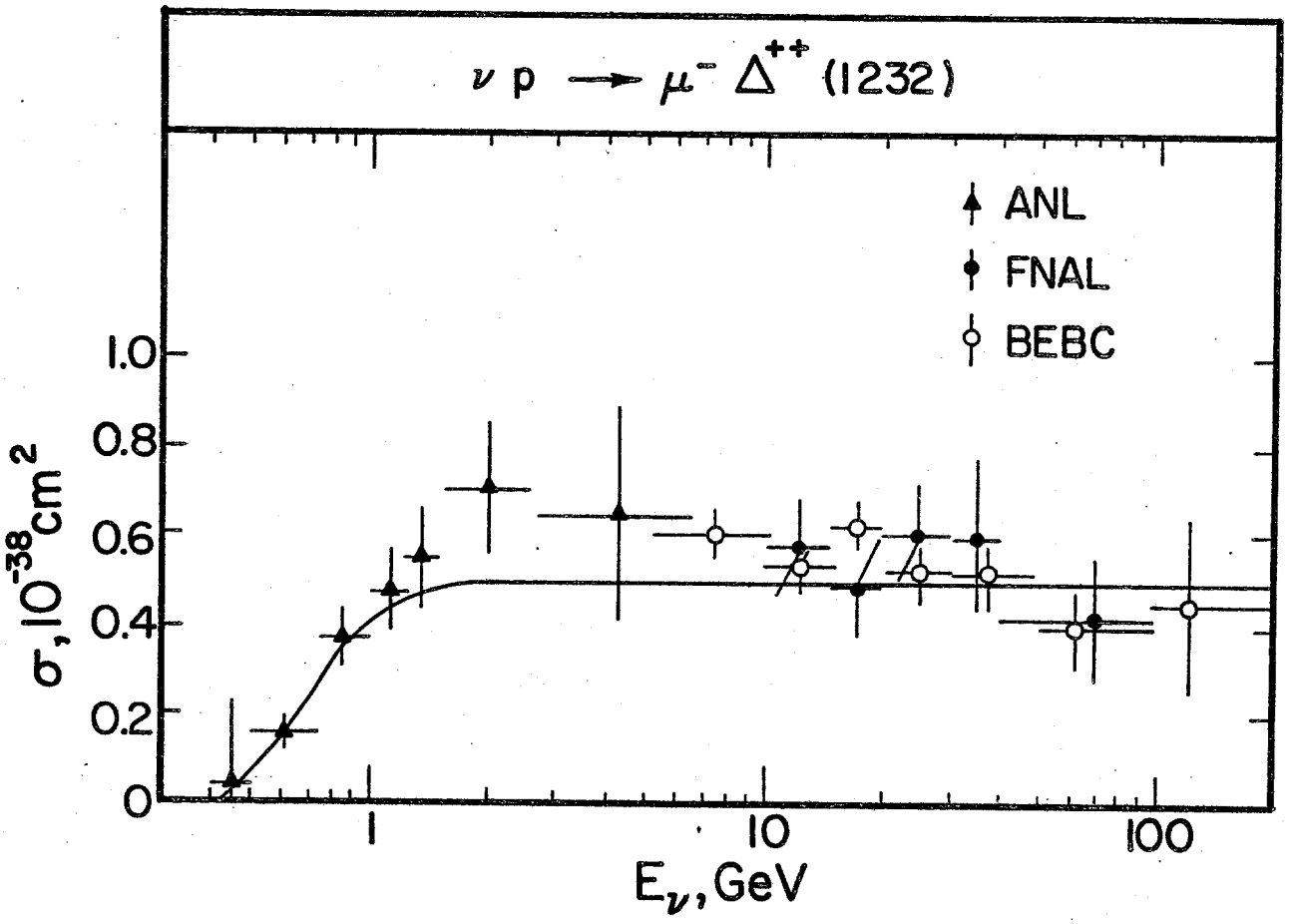
$\nu p \rightarrow \mu^- \Delta^{++}(1232)$
ANL
FNAL
BEBC
1.0
0.8
0.6
0.4
0.2
0
$\sigma, 10^{-38} cm^2$
1
10
100
E_ν, GeV

Fig. 11

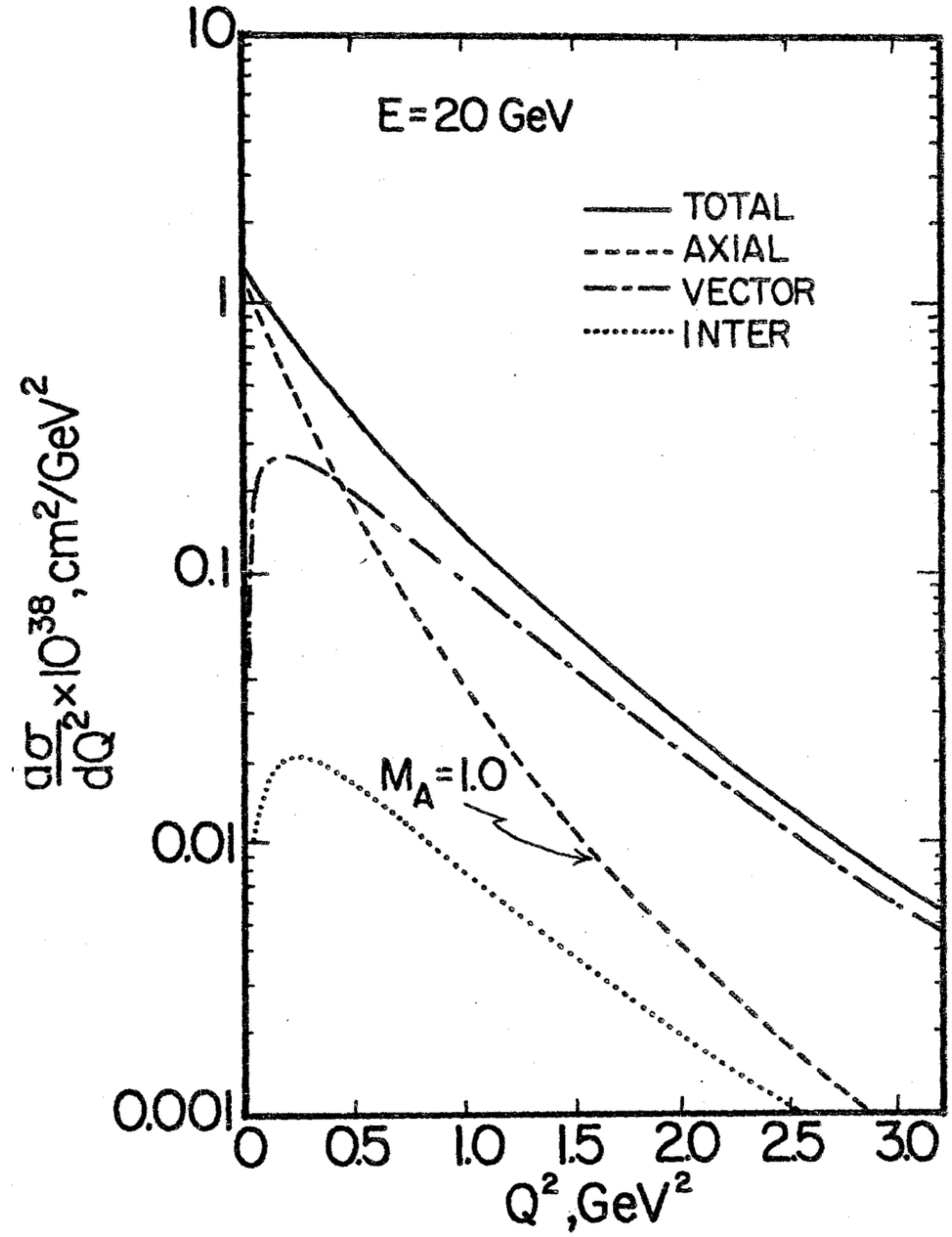
10
1
0.1
0.01
0.001
E=20 GeV
TOTAL
AXIAL
VECTOR
INTER
M_A=1.0
$\frac{d\sigma}{dQ^2} \times 10^{38}$, cm^2/GeV^2
0
0.5
1.0
1.5
2.0
2.5
3.0
Q^2, GeV^2

Fig. 12

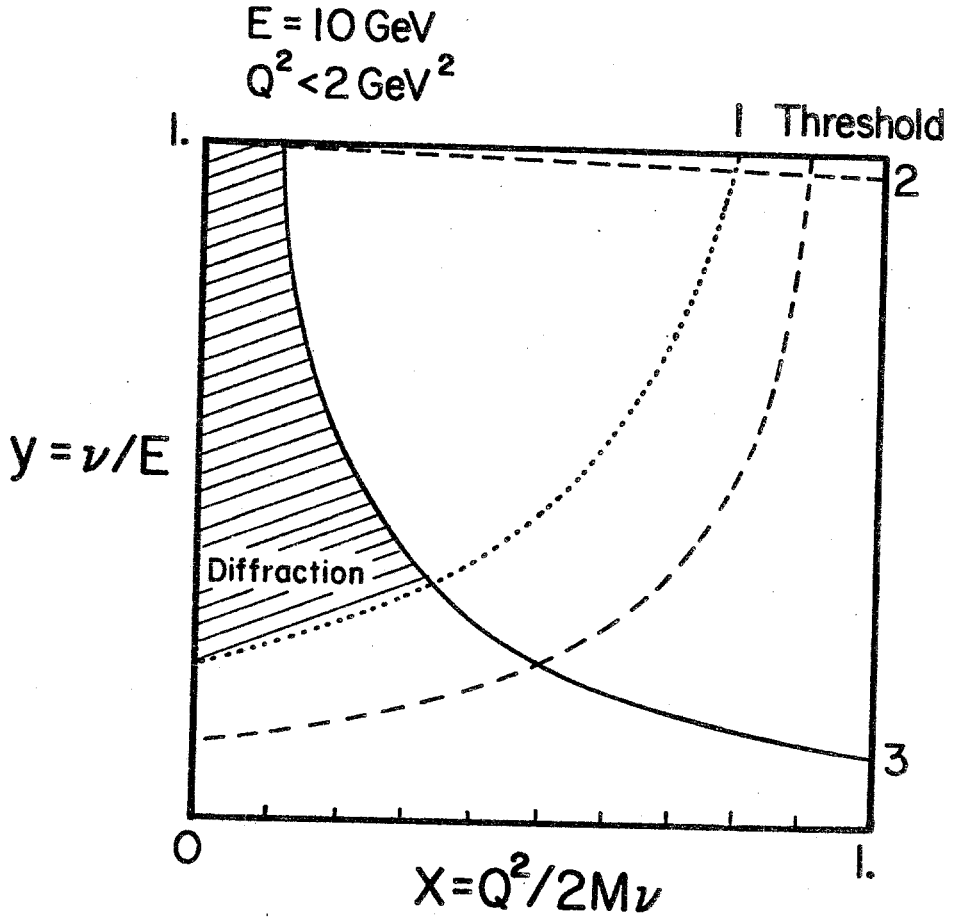
E = 10 GeV
$Q^2 < 2\ GeV^2$
1.
1 Threshold
2
3
$y = \nu/E$
Diffraction
0
1.
$X = Q^2/2M\nu$

Fig. 13

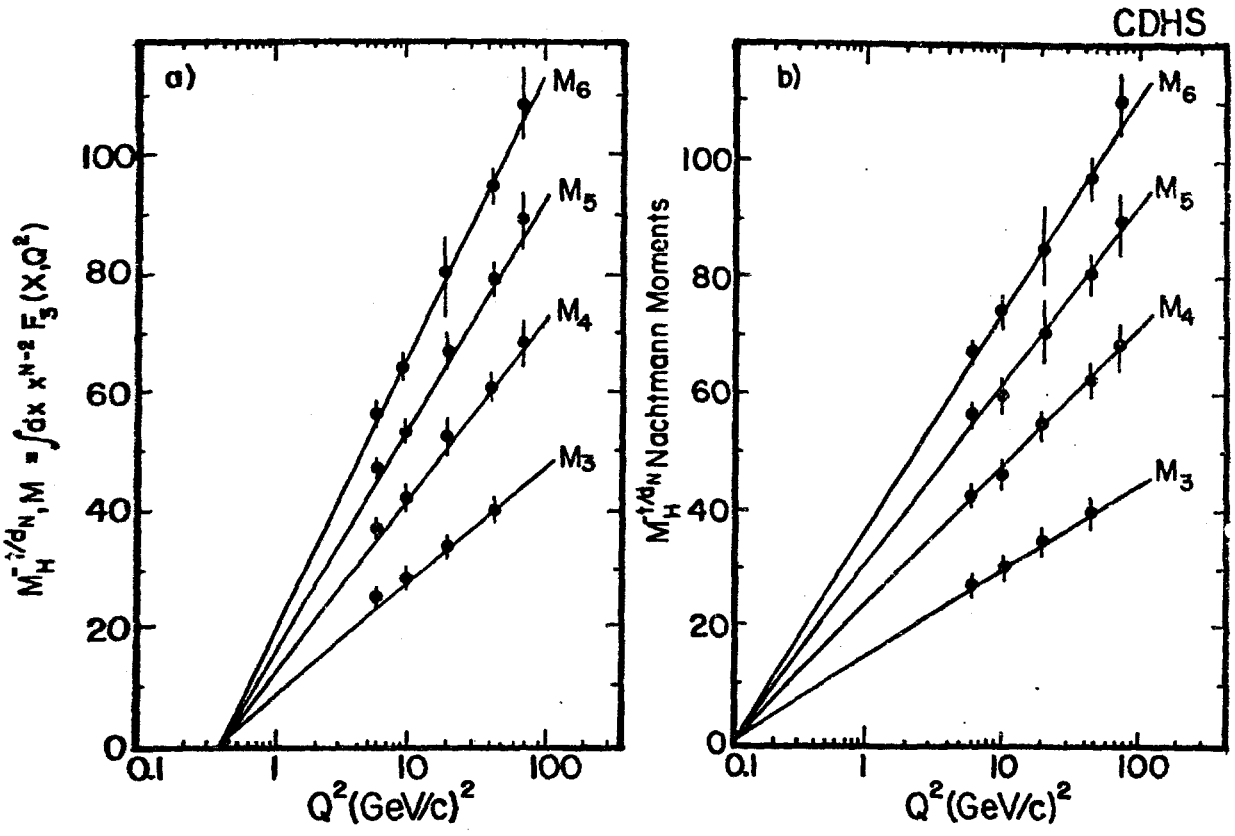
CDHS
a)
b)
M_6
M_5
M_4
M_3
$M_H^{n/d_N,M} = \int dx\, x^{N-2} F_3(X,Q^2)$
M_H^{n/d_N} Nachtmann Moments
Q^2(GeV/c)^2
0
20
40
60
80
100
0.1
1
10
100

Fig. 14

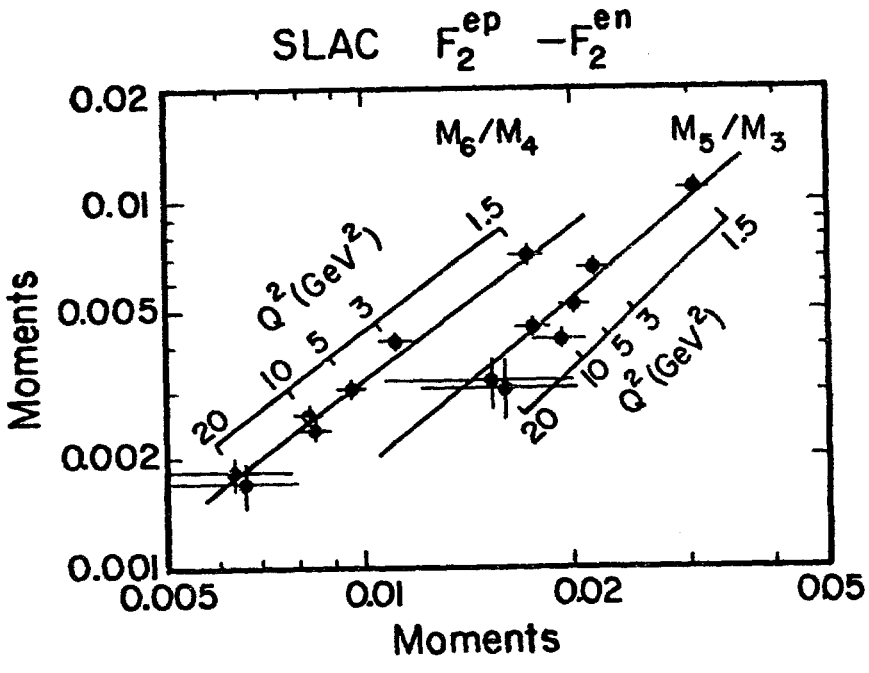
SLAC $F_2^{ep} - F_2^{en}$
M_6/M_4
M_5/M_3
Q^2(GeV^2)
1.5
3
5
10
20
Moments
0.001
0.002
0.005
0.01
0.02
0.05

Fig. 15

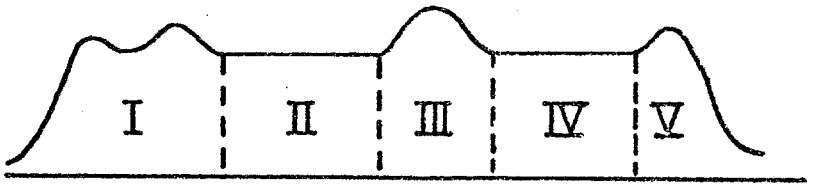

$$y^* = \frac{1}{2} \ln \left[(E^* + p_L^*) / (E^* - p_L^*) \right]$$

Fig. 16

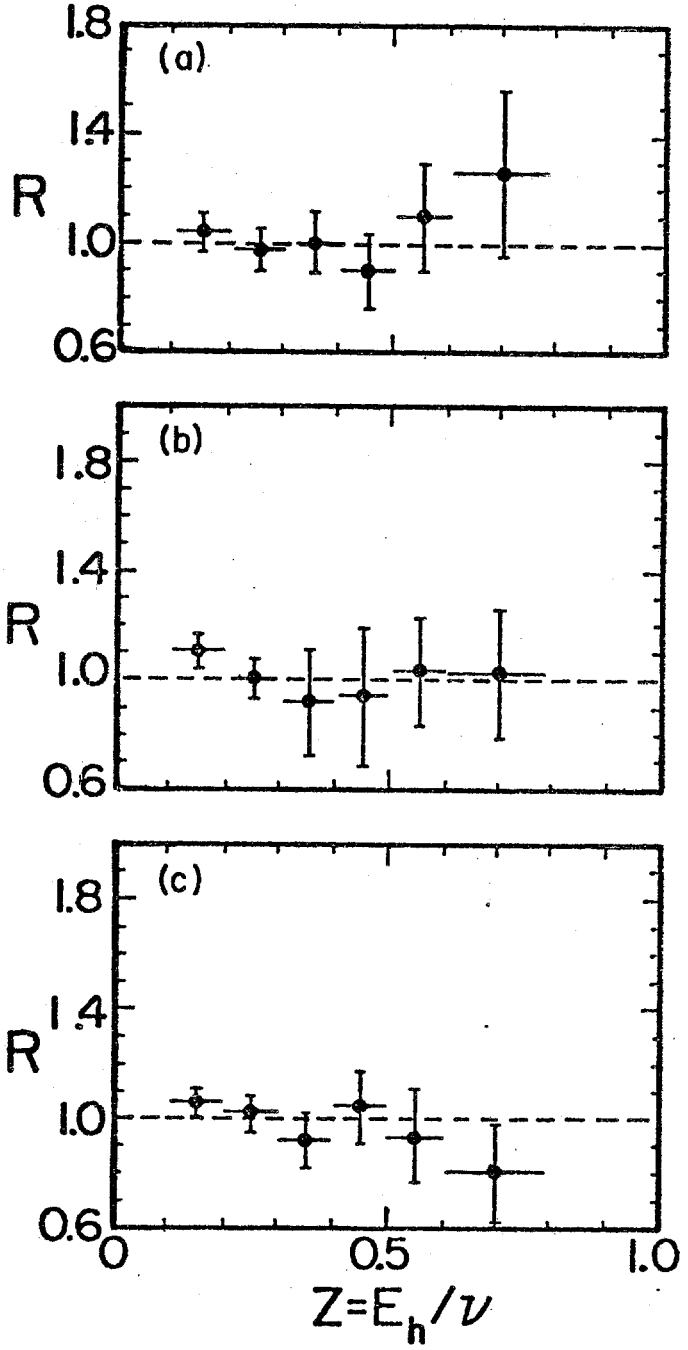

Fig. 17

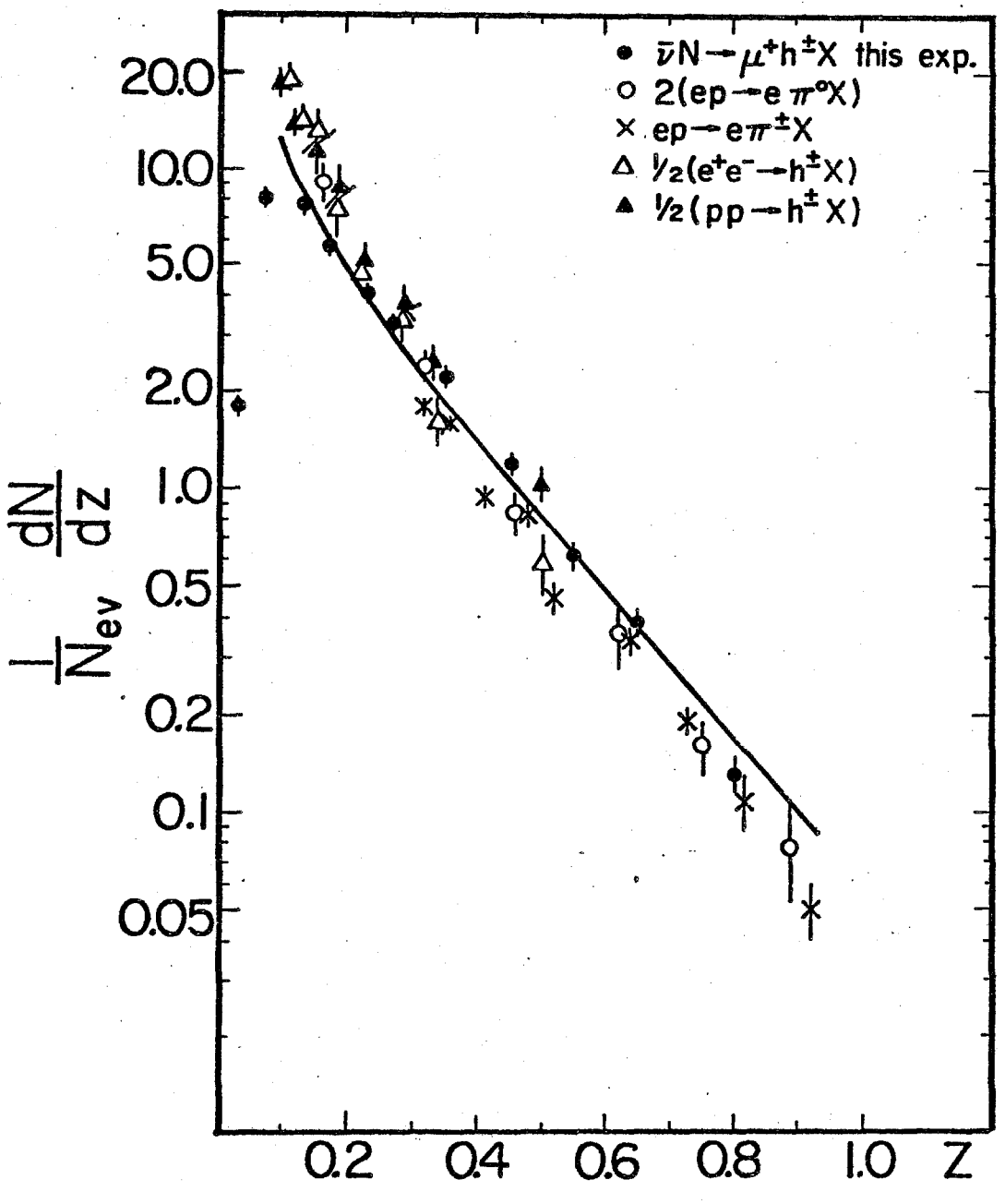
$\bar{\nu}N \to \mu^+ h^\pm X$ this exp.
$2(ep \to e\pi^0 X)$
$ep \to e\pi^\pm X$
$\frac{1}{2}(e^+e^- \to h^\pm X)$
$\frac{1}{2}(pp \to h^\pm X)$
$\frac{1}{N_{ev}} \frac{dN}{dz}$
20.0
10.0
5.0
2.0
1.0
0.5
0.2
0.1
0.05
0.2
0.4
0.6
0.8
1.0
Z

Fig. 18

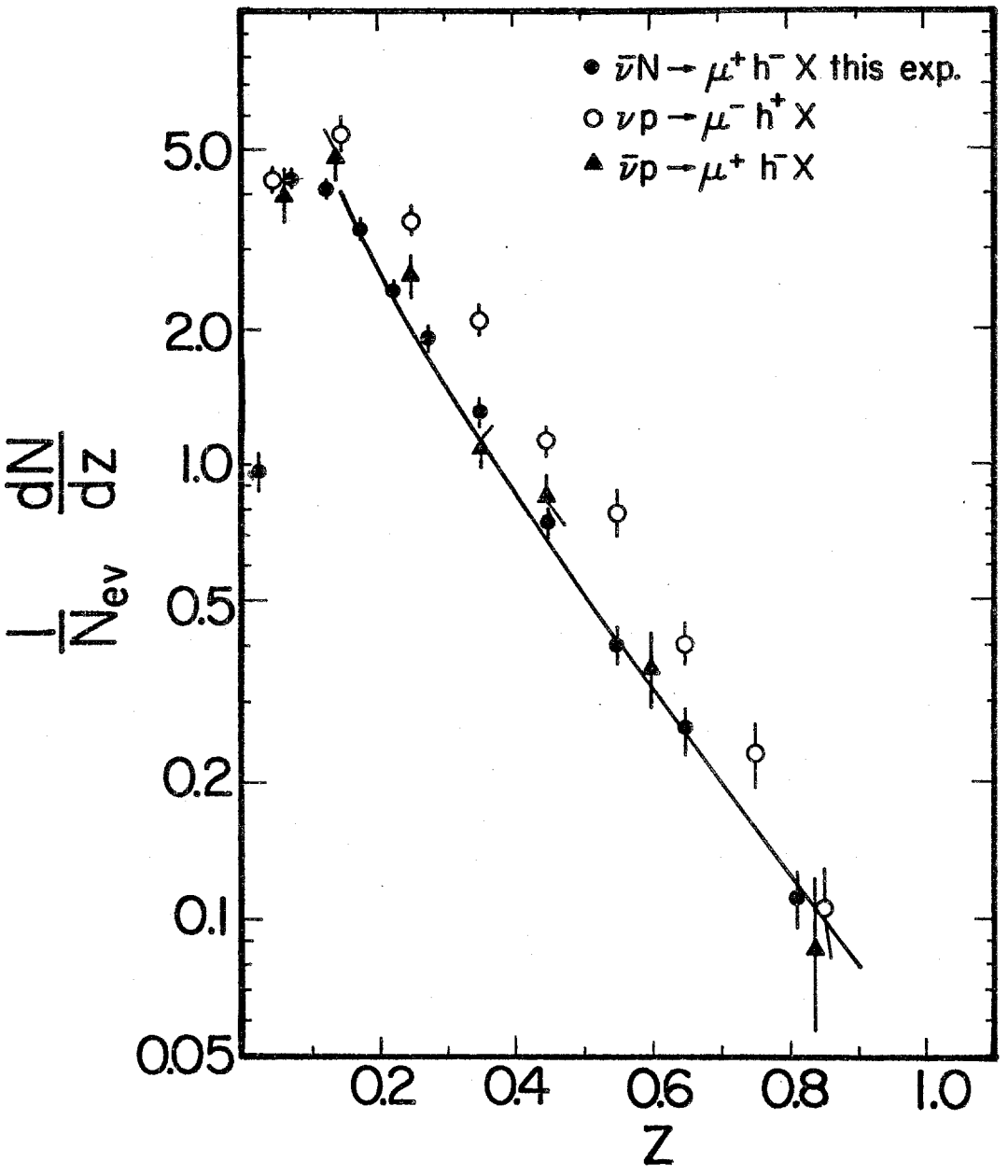
● $\bar{\nu}N \rightarrow \mu^+ h^- X$ this exp.
○ $\nu p \rightarrow \mu^- h^+ X$
▲ $\bar{\nu}p \rightarrow \mu^+ h^- X$
$\frac{1}{N_{ev}} \frac{dN}{dz}$
5.0
2.0
1.0
0.5
0.2
0.1
0.05
0.2
0.4
0.6
0.8
1.0
Z

Fig. 19

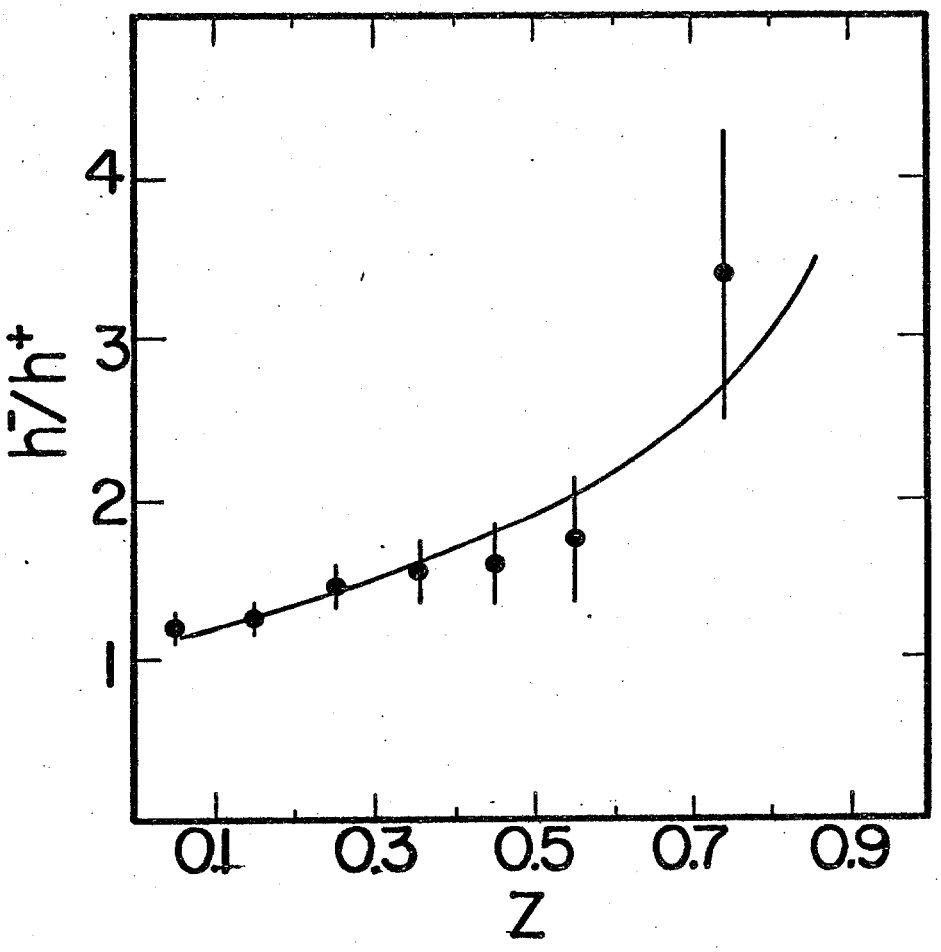
h^-/h^+
4
3
2
1
0.1
0.3
0.5
0.7
0.9
Z

Fig. 20

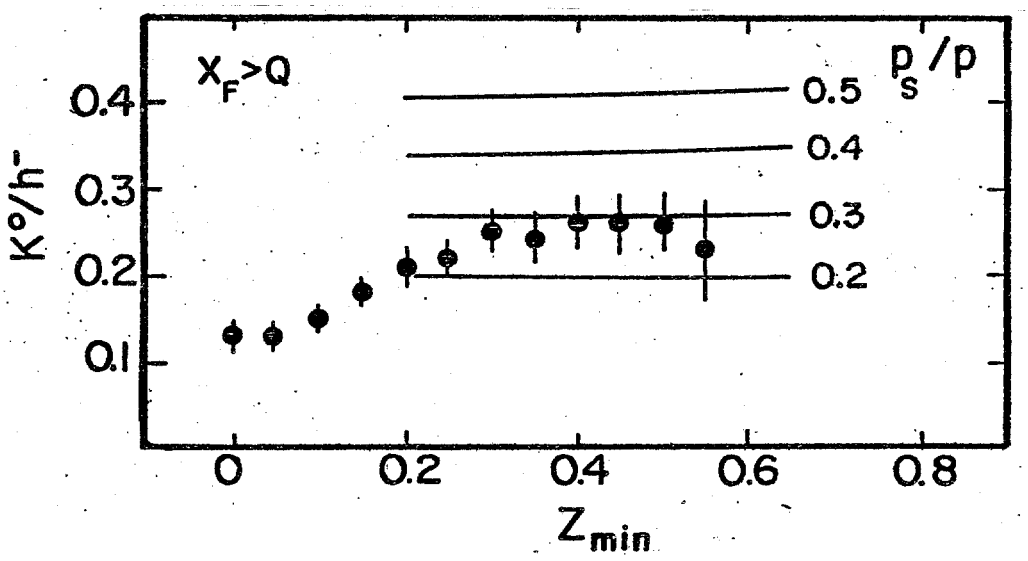
$X_F>0$
p_s/p
0.5
0.4
0.3
0.2
K^o/h^-
0.4
0.3
0.2
0.1
0
0.2
0.4
0.6
0.8
Z_{min}

Fig. 21

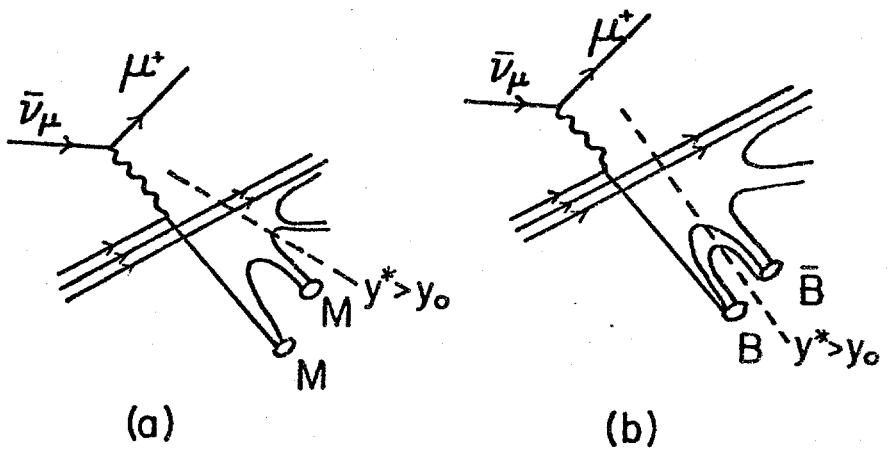

Fig. 22

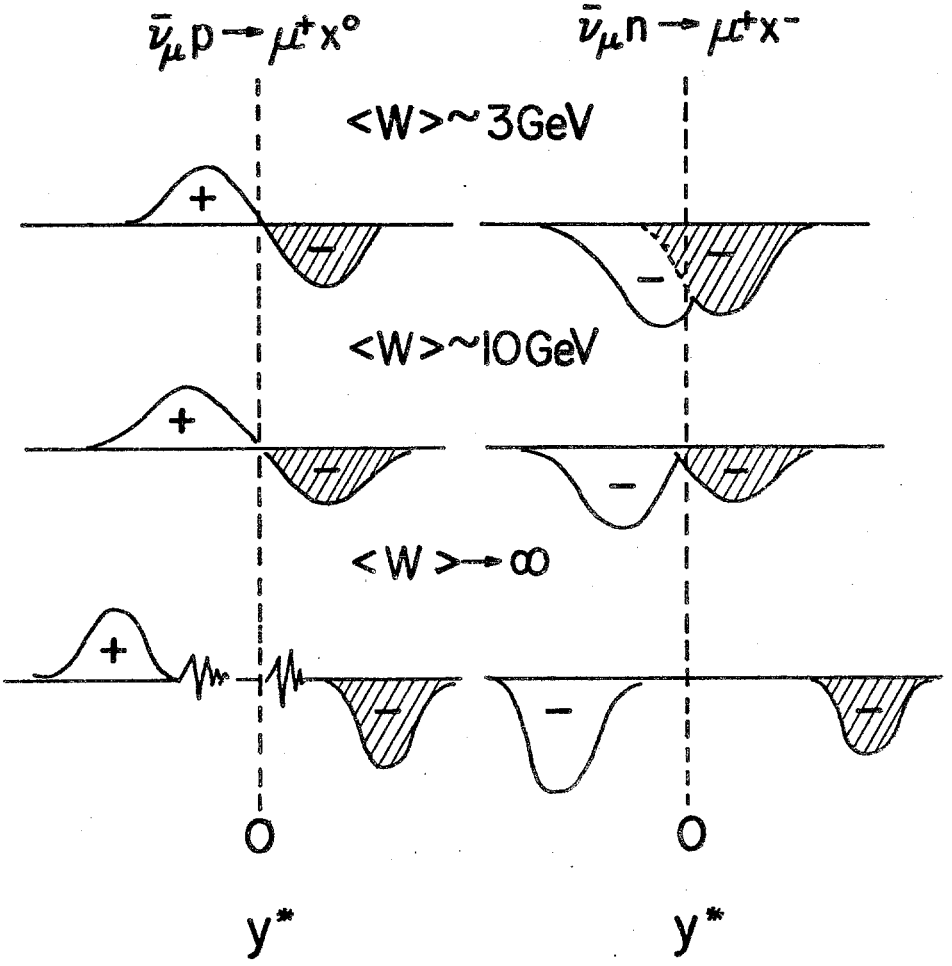

Fig. 23

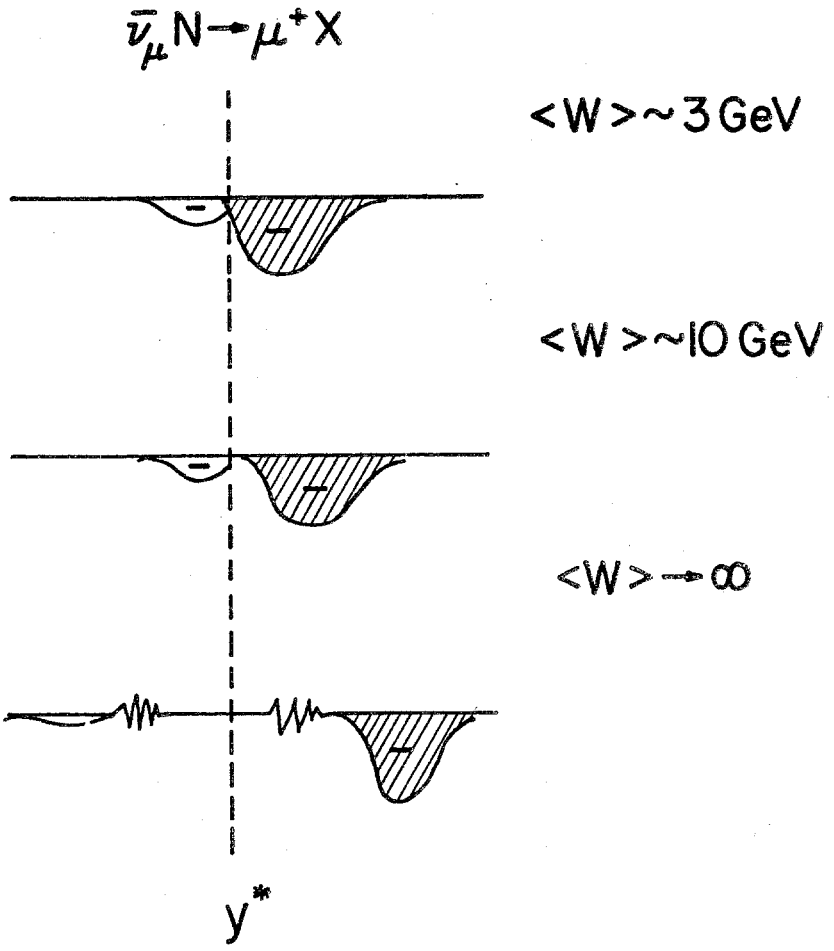
$\bar{\nu}_\mu N \to \mu^+ X$
$\langle W \rangle \sim 3$ GeV
$\langle W \rangle \sim 10$ GeV
$\langle W \rangle \to \infty$
y^*

Fig. 24

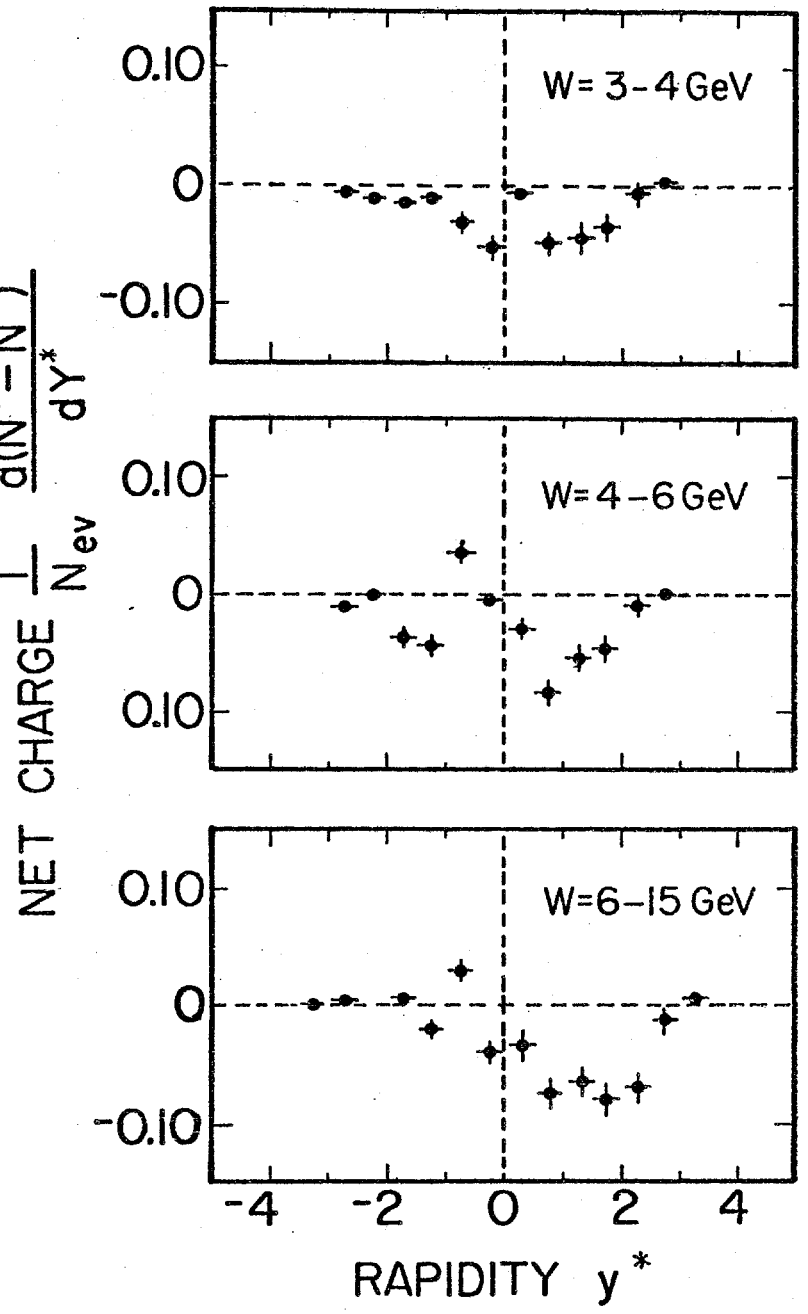
W= 3-4 GeV
W= 4-6 GeV
W=6-15 GeV
0.10
0
-0.10
-4
-2
0
2
4
RAPIDITY y*
NET CHARGE 1/N_ev d(N+ - N-)/dY*

Fig. 25

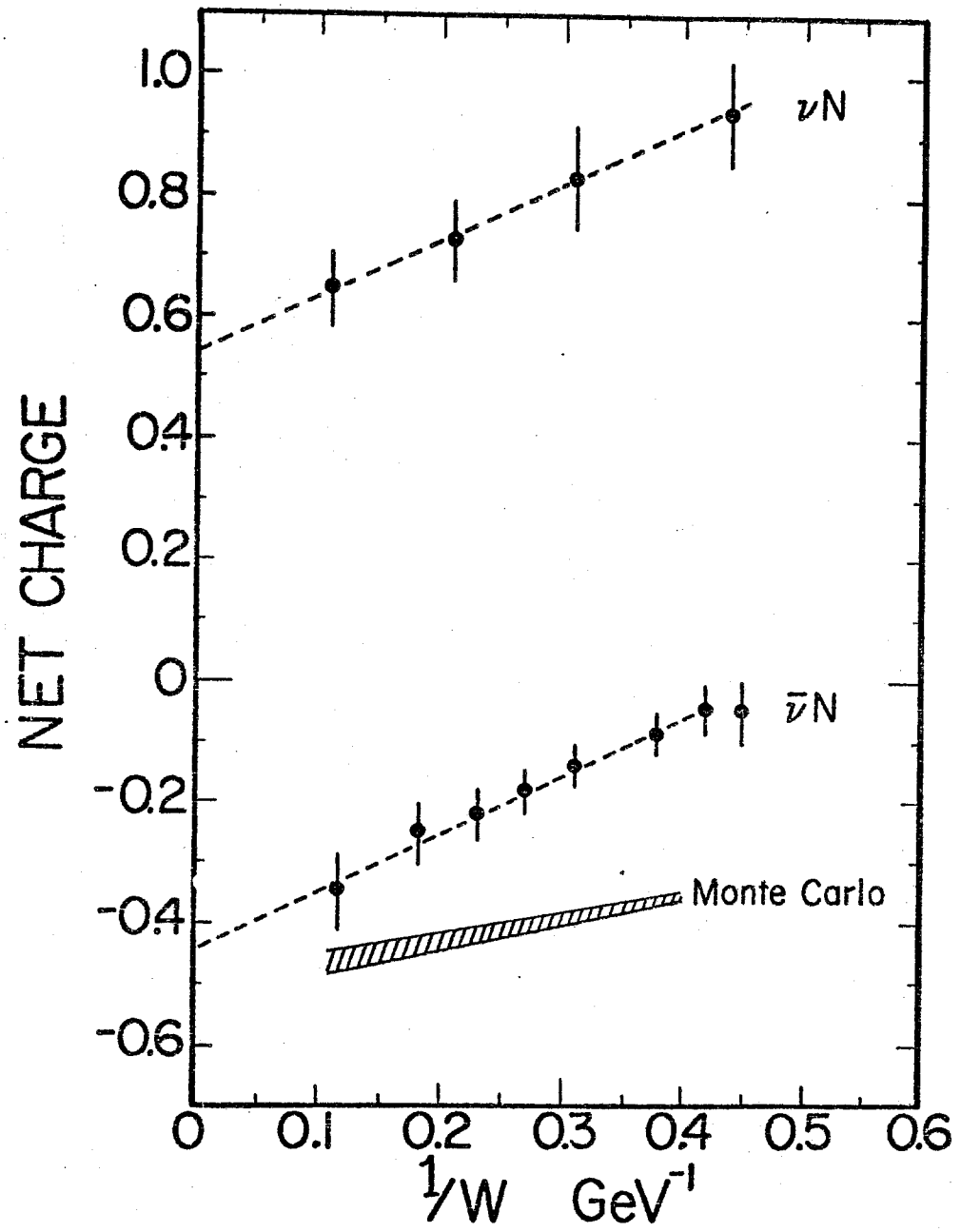
NET CHARGE
1.0
0.8
0.6
0.4
0.2
0
-0.2
-0.4
-0.6
νN
ν̄N
Monte Carlo
0
0.1
0.2
0.3
0.4
0.5
0.6
1/W GeV⁻¹

Fig. 26

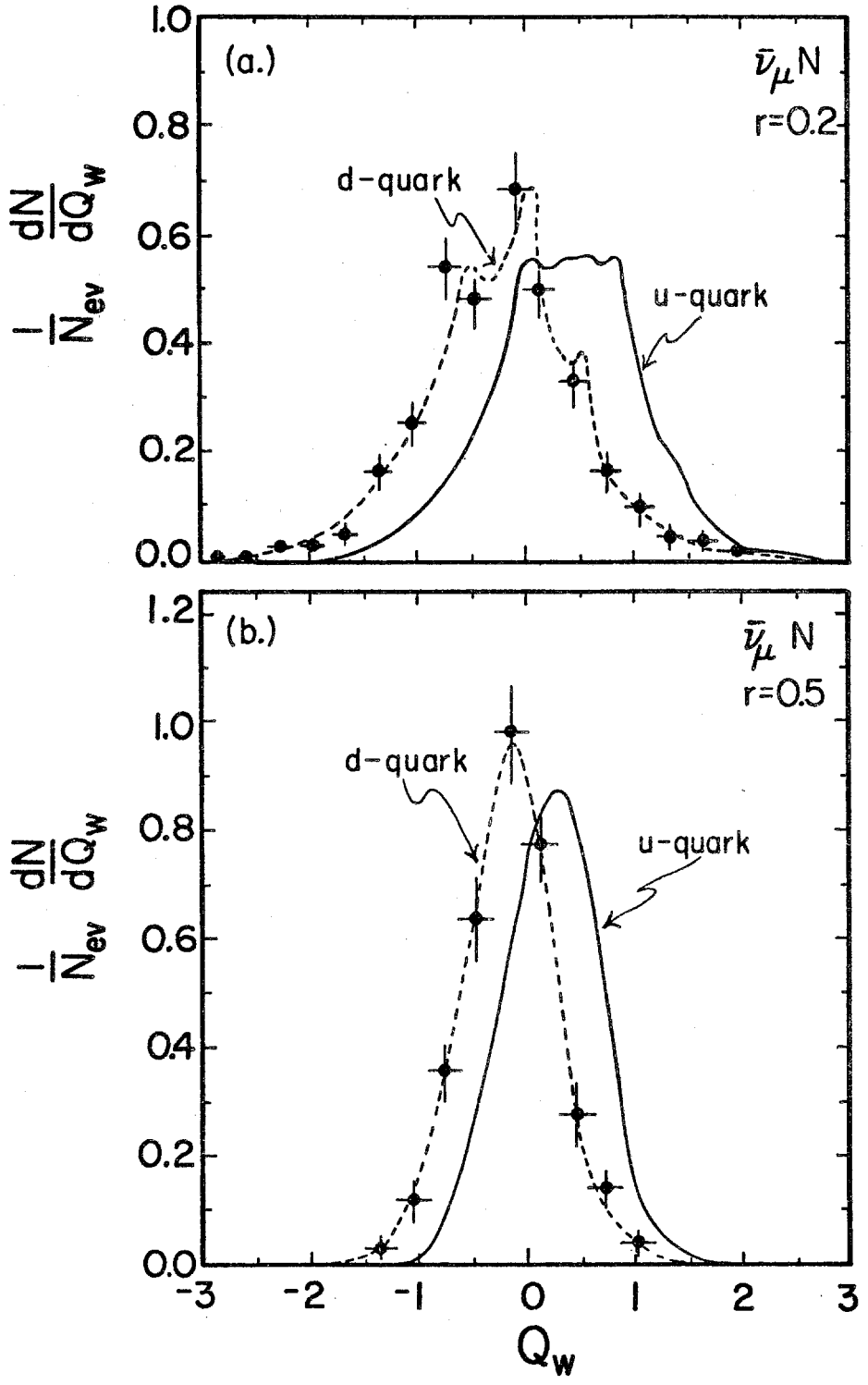
(a.)
$\bar{\nu}_\mu N$
r=0.2
d-quark
u-quark
(b.)
$\bar{\nu}_\mu$ N
r=0.5
d-quark
u-quark
$\frac{1}{N_{ev}}\frac{dN}{dQ_w}$
Q_w
1.0
0.8
0.6
0.4
0.2
0.0
1.2
-3
-2
-1
0
1
2
3

Fig. 27

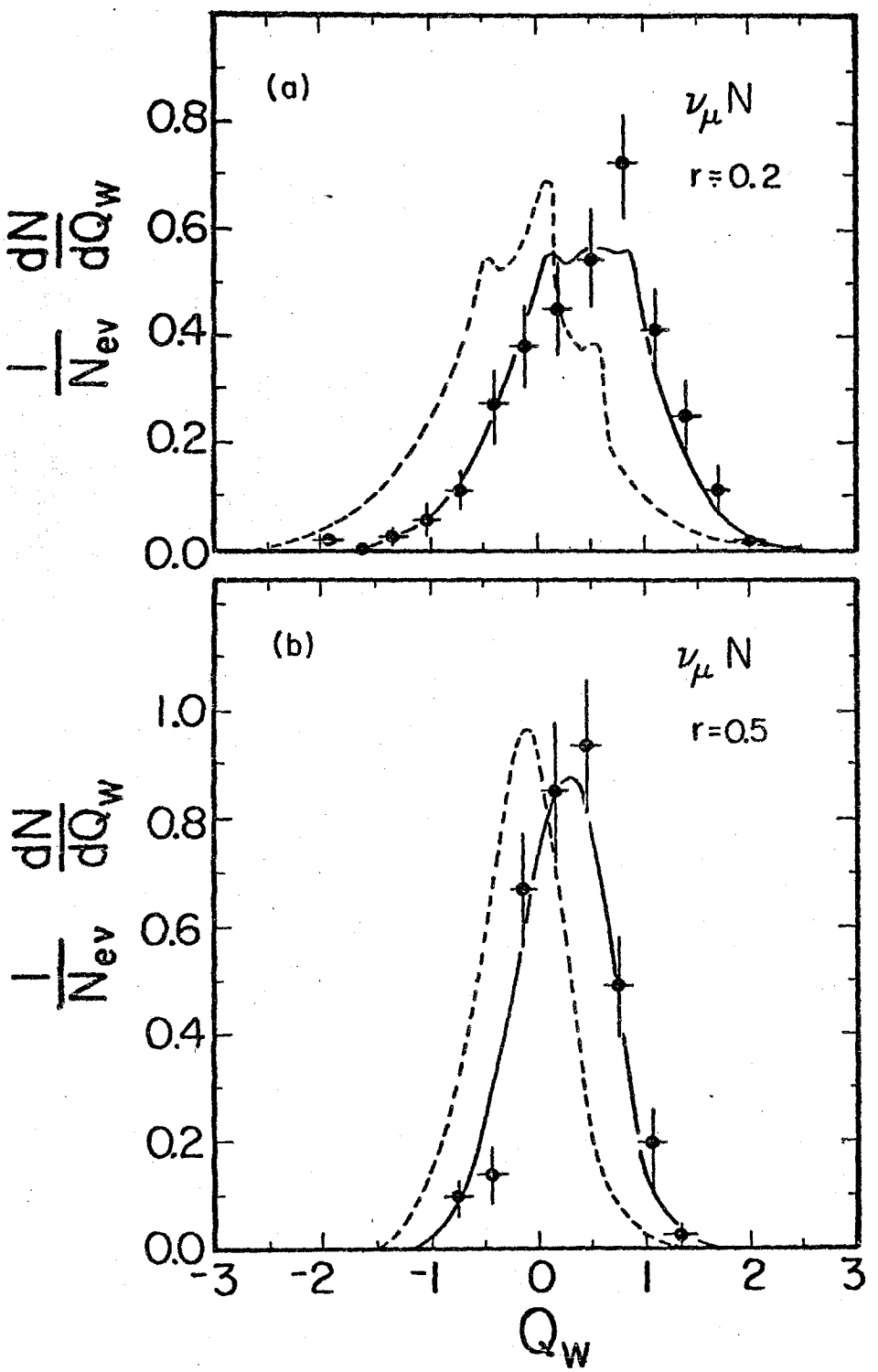
(a)
ν_μN
r=0.2
(b)
ν_μN
r=0.5
$\frac{1}{N_{ev}}\frac{dN}{dQ_W}$
0.0
0.2
0.4
0.6
0.8
1.0
-3
-2
-1
0
1
2
3
Q_W

Fig. 28

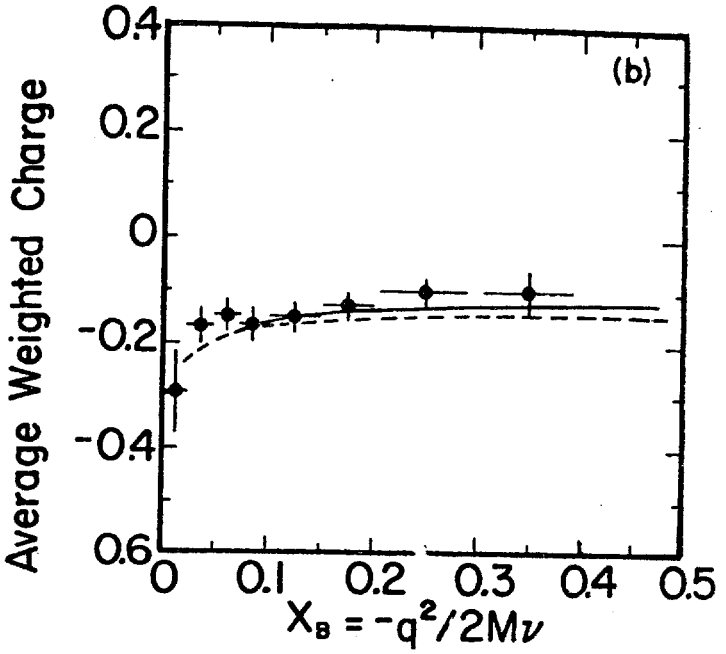
(b)
Average Weighted Charge
0.4
0.2
0
-0.2
-0.4
-0.6
0
0.1
0.2
0.3
0.4
0.5
$X_B = -q^2/2M\nu$

Fig. 29

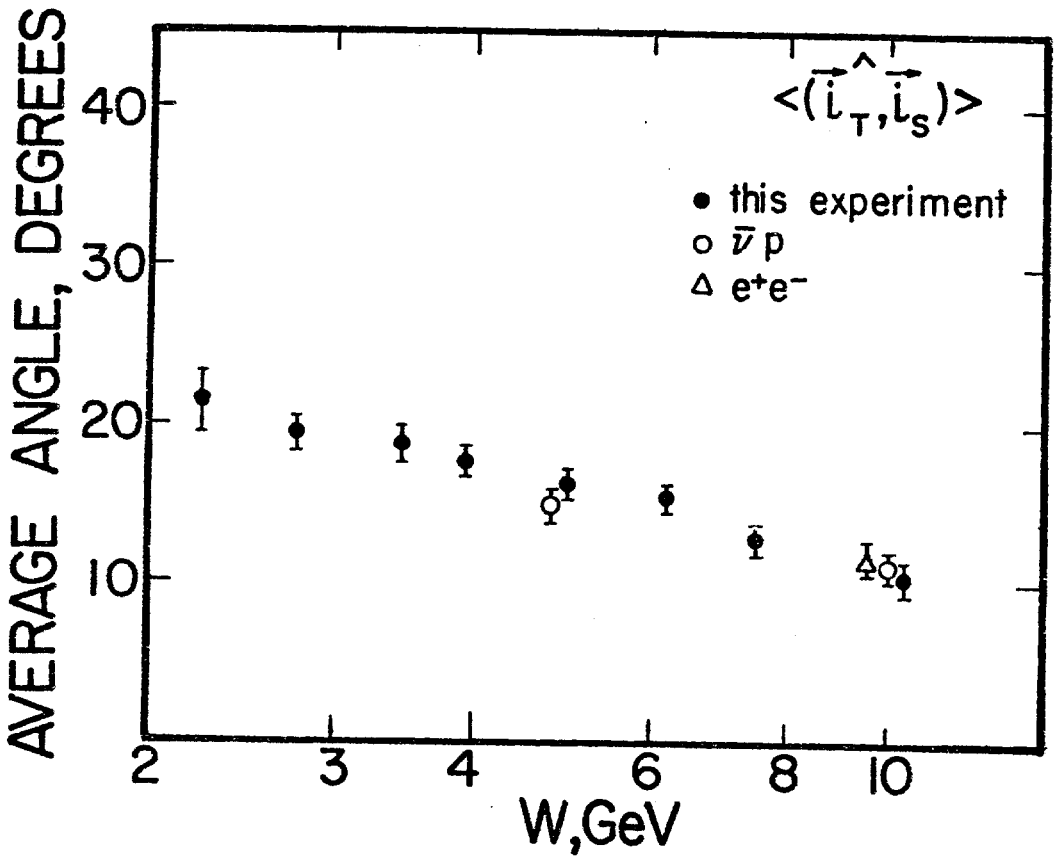
AVERAGE ANGLE, DEGREES
40
30
20
10
2
3
4
6
8
10
W,GeV
$\langle(\hat{\vec{i}}_T, \vec{i}_S)\rangle$
• this experiment
o $\bar{\nu}$ p
Δ e^+e^-

Fig. 30

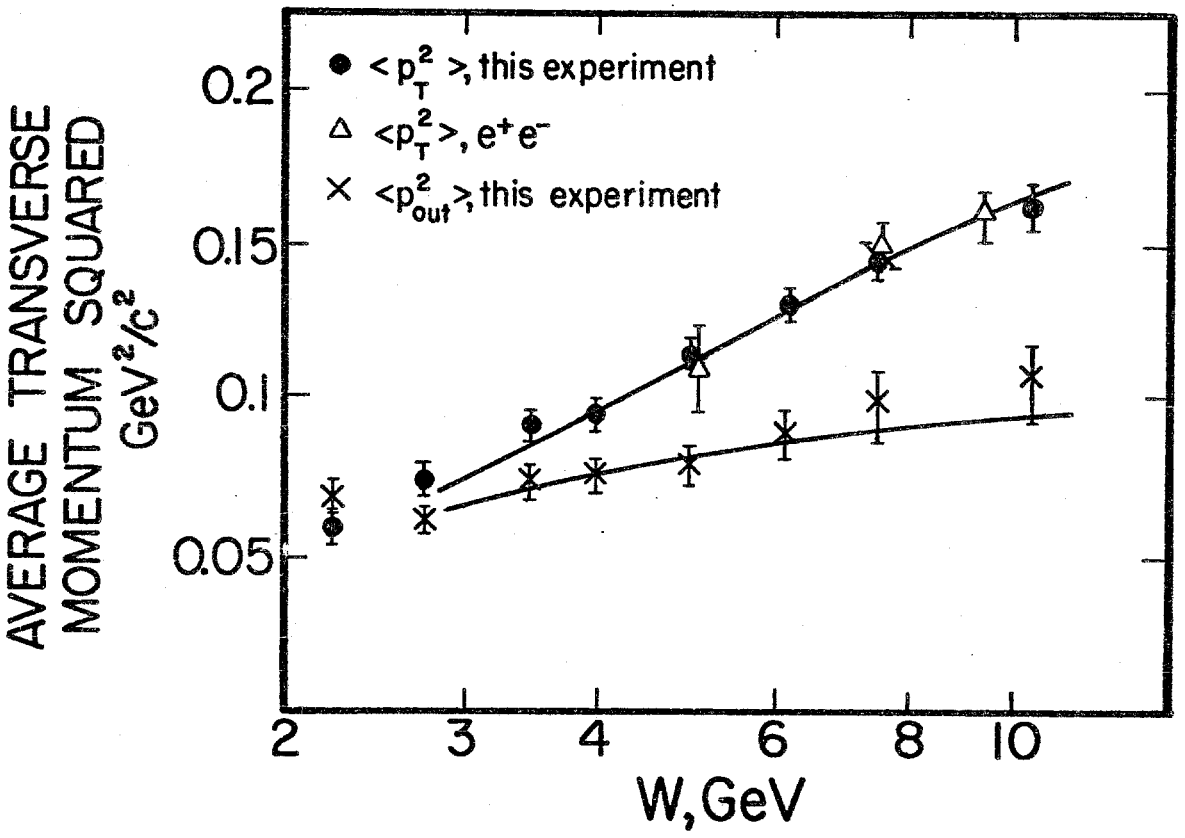
AVERAGE TRANSVERSE MOMENTUM SQUARED
GeV²/c²
0.2
0.15
0.1
0.05
● <p²T>, this experiment
△ <p²T>, e⁺e⁻
× <p²out>, this experiment
2
3
4
6
8
10
W, GeV

Fig. 31

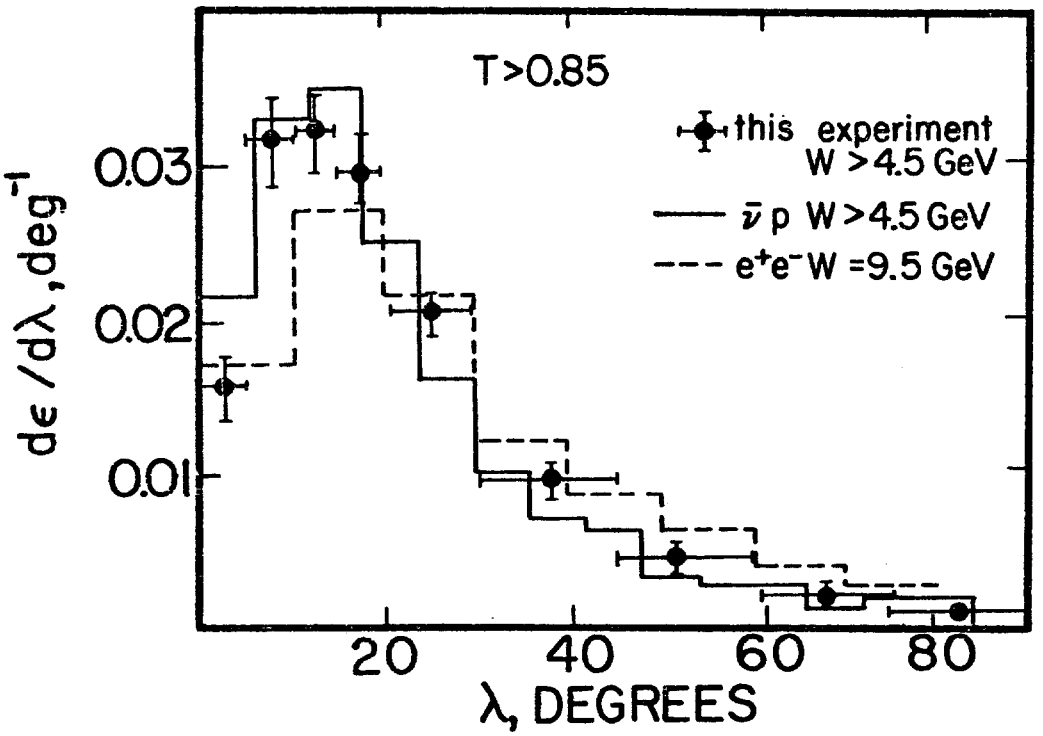
T>0.85
this experiment
W >4.5 GeV
$\bar{\nu}$ p W>4.5 GeV
e⁺e⁻ W =9.5 GeV
dε /dλ ,deg⁻¹
0.03
0.02
0.01
20
40
60
80
λ, DEGREES

Fig. 32

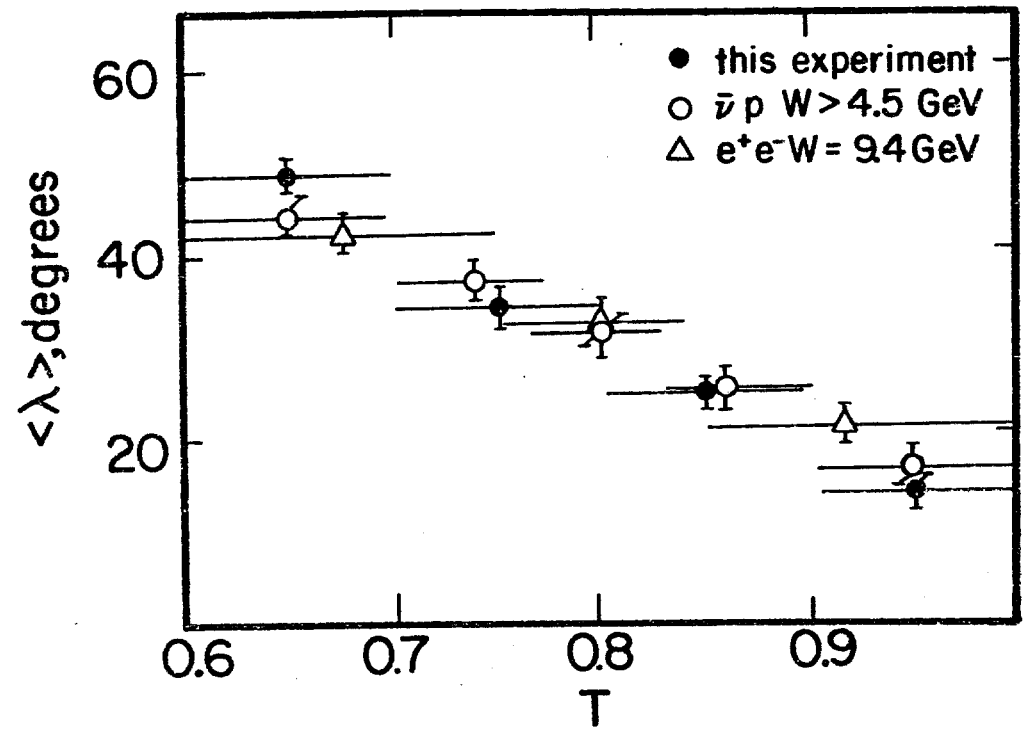
this experiment
$\bar{\nu}$ p W>4.5 GeV
e⁺e⁻ W= 9.4 GeV
<λ>,degrees
60
40
20
0.6
0.7
0.8
0.9
T

Fig. 33